Contents lists available at ScienceDirect

Geomechanics for Energy and the Environment

Applied stress reduces swelling of coal induced by adsorption of water

Jinfeng Liu [a,b,*], Peter A. Fokker [b,c], Colin J. Peach [b], Christopher J. Spiers [b]

[a] Guangdong Provincial Key Lab of Geodynamics and Geohazards, School of Earth Sciences and Engineering, Sun Yat-sen University, 510275, Guangzhou, China
[b] Department of Earth Sciences, Faculty of Geosciences, Utrecht University, 3584CD Utrecht, The Netherlands
[c] Netherlands Institute of Applied Geosciences, TNO—National Geological Survey, Utrecht, The Netherlands

ARTICLE INFO

ABSTRACT

This paper investigates whether or not applied stress reduces swelling of coal upon water adsorption, and, if so, what mechanisms are responsible. With this aim, thermodynamic models were developed addressing the effect of a general applied stress on water adsorption capacity and associated swelling behaviour of coal matrix material, assuming monolayer, multilayer and mixed mono/multilayer adsorption mechanisms. These all predict applied stress reduces water adsorption capacity and hence swelling. Experiments were performed on both a solid disc and on pre-compacted powders of Brzeszcze high volatile bituminous coal at a constant temperature (40 °C), using a uniaxial compaction apparatus. The mechanical response of the samples to stepwise axial loading was determined under both evacuated and water-exposed conditions. The evacuated samples showed reversible, elastic behaviour. Water-exposed samples exhibited elastic deformation, time-dependent reversible deformation, plus plastic strains with time-dependent processes. Axial swelling strains upon introduction of distilled water at a constant fluid pressure (0.1 MPa) were also measured for samples subjected to fixed axial stresses (25–100 MPa). The results demonstrated the applied stress reduces swelling upon water adsorption. Comparison with predictions made using the three models shows that stress-driven reduction in sorption-induced swelling is caused by the combined effects of (a) permanent time-dependent (compressive) deformation (creep), (b) the thermodynamic effect of a stress-driven reduction in water sorption capacity and (c) stress-driven closure of transport paths within the coal matrix. Nonetheless, our results show the above effects of stress on the swelling response of (Brzeszcze) high volatile bituminous coal to water are minor at typical in-situ stresses (10–30 MPa). This suggests the large shrinkage effect of the coal upon drying that has been observed in unconfined experiments is not changed by in-situ stresses.

© 2018 Elsevier Ltd. All rights reserved.

1. Introduction

Subsurface coal seams generally consist of low permeability coal matrix material cross cut by a multiscale network of joints or cleats.[1–3] These systems often contain large amounts of methane (CH_4) and water, in part trapped in fluid form in the cleat system but mostly trapped in adsorbed form in the nanoporous coal matrix.[4] Primary production of coalbed methane (CBM) is typically accomplished by reducing the pressure of pore water trapped in the cleat system. Methane then desorbs from the coal matrix as the pressure transmitted to free methane present in the cleats falls below the fluid pressure measured with respect to the adsorbed methane content at local equilibrium.[4,5] However, the rate of transport from the low permeability coal matrix into the cleat system

generally limits primary CBM production by pressure depletion methods to 20%–60% of the estimated reserves, leaving 40%–80% of the methane initially present in place.[4] Besides this residual methane, pressure depletion also leaves large amounts of water trapped in the coal matrix via sorption.[4]

Sorption of both methane and water by coal matrix material leads to several percent swelling (∼1%–5% at maximum), while desorption produces similar shrinkage.[6–9] Against this background, removing water and CH_4 from coal seams by injection of dry N_2 has recently been suggested as a possible method of secondarily enhancing CBM recovery (ECBM).[4,5,10] This concept is based on the fact that (a) the swelling of coal upon adsorption of N_2 is around half of that occurring upon adsorption of CH_4 at similar *PT* conditions,[11,12] and (b) the swelling/shrinkage response of coal to adsorption and desorption of water (1%–5% at 100% relative humidity) is similar to that caused by adsorption and desorption of CH_4 at a pressure of 10 MPa (1%–3%).[10,13] The implication is that injection of dry N_2 into a depleted coalbed methane reservoir,

---

* Corresponding author at: Guangdong Provincial Key Lab of Geodynamics and Geohazards, School of Earth Sciences and Engineering, Sun Yat-sen University, 510275, Guangzhou, China.
E-mail address: liujinf5@mail.sysu.edu.cn (J. Liu).

followed by on-going flushing, may be capable of initiating self-enhancing shrinkage and (micro)cracking of the coal, hence enhanced methane production, as methane and water are progressively removed and replaced by sorbing N_2.[10,12,14] Understanding swelling/shrinkage effects in coal due to adsorption and desorption of water, under in-situ conditions of temperature, water activity (i.e. partial pressure or relative humidity, RH) and rock stress is therefore of direct importance for designing and optimizing enhanced (E)CBM production strategies.

Recent experiments on swelling of coal due to water vapour adsorption have demonstrated that the equilibrium swelling strain is linearly proportional to the concentration of adsorbed water molecules,[6,7] and to the imposed relative humidity or activity of water vapour.[6,10] It has also been shown that transient, time-dependent swelling, following a change in RH, is controlled by diffusion of water molecules.[10] However, little attention has been paid in the literature to the effect of in-situ rock stress on water sorption and the associated swelling. Such effects may nonetheless be important under subsurface conditions, bearing in mind that the applied stress is known to reduce the sorption capacity of coal with respect to CO_2 and CH_4. This has been demonstrated experimentally[3,13,15,16] and predicted theoretically via thermodynamic models addressing the stress–strain–sorption behaviour of coal, as developed by Hol et al.[3,16] (see also Vandamme et al.[17] and Liu et al.[13]). These models show that the additional stress–strain work done, due to sorption-induced swelling of coal matrix material against an applied (rock) stress, increases the chemical potential of the adsorbed molecules and hence reduces sorption capacity. As the theory applies in its broad lines to any solid sorbent plus sorbate system, it follows that the in-situ stress pertaining in coal seams will likely reduce the sorption capacity of coal with respect to water, hence reducing the sorption-induced swelling response. Strictly, however, the theory assumes monolayer (discrete site) adsorption behaviour of the sorbate molecules, whereas adsorption of water by coal, unlike adsorption of CH_4 and CO_2, is widely accepted to involve multiple layer adsorption.[18–22] To understand the effects of stress on water sorption and associated swelling, under conditions corresponding to thermodynamic equilibrium, the existing monolayer theory needs to be extended to cover multilayer adsorption. On the other hand, equilibrium thermodynamic models for stress–strain–sorption behaviour may not apply on the coal seam scale, as changes in coal stress state might close or open pre-existing micropore or (micro)fracture networks inside the coal, changing the accessibility of water to the coal matrix and preventing homogeneous equilibration.[3,15,23,24] Permanent deformation and creep effects might also occur when wet coal experiences changing long-term stress states.[25] To gain insight into the influence of applied stress on the swelling behaviour of coal upon adsorption of water, progress is needed in understanding all of these effects.

In this study, we attempt to determine whether or not applied stress influences the swelling response of coal caused by exposure to and adsorption of water, and, if so, to determine the mechanisms responsible. To achieve this, we first extend our previous thermodynamic model[13] for the stress–strain–sorption behaviour of coal matrix material to address not only monolayer but also multiple layer adsorption of water. We then report the results of experiments designed to determine the effects of applied stress on swelling strain development in coal samples exposed to distilled water at atmospheric pressure (0.1 MPa). The experiments were performed on both coal disc and pre-compacted powder samples at a constant temperature of 40 °C and at applied stresses in the range 25–100 MPa, using a uniaxial compaction apparatus.

2. Thermodynamic models for swelling of coal matrix material due to adsorption of water under a general stress state σ_{ij}

2.1. Starting assumptions

Throughout our analysis, compressive stresses and fluid pressure are measured positive, as is swelling strain. Following Liu et al.,[13] we begin by considering a small coal matrix cube of mass m and side l ($\leq$ 1 mm) (density ρ, kg/m^3), surrounded by water vapour or liquid water present at constant pressure P, absolute temperature T, and chemical potential μ_g. The coal matrix cube, also at uniform temperature T, is independently subjected to a general stress state σ_{ij} via a permeable loading frame that allows free access of water vapour or water to the coal. The cube is considered homogeneous in structure and composition at the particle length scale l, but may be anisotropic in properties. It is further assumed to contain nano-pores only, so that there is no Darcian flow and negligible storage of free (unadsorbed) gas. In other words, the coal particle is so small that it is cleat free and can take up water only by molecular diffusion and adsorption.[26] This further means that only a few unadsorbed molecules exist in the nanopores, and that therefore they do not behave as a fluid phase. The coal particle is accordingly elastic but not poro-elastic.[27]

Previous studies employing experimental approaches (such as sorption tests coupled with infrared spectroscopy and ionic thermal current measurements) and thermodynamic/kinetic modelling methods[20,21,28–33] show that water molecules are primarily trapped by oxygen-bearing functional groups (mostly by carboxyl groups) present in the coal matrix via hydrogen bonds. Water thus adsorbed forms a first layer of adsorbed molecules, having high binding energy due to a strong interaction between the active functional groups and the adsorbed molecules.[20–22,31,32] These adsorbed water molecules then form secondary sites for attachment of additional water molecules via hydrogen bonds with lower binding energy.[21,33,34] Based on experimental findings that the volumetric swelling strains of coals (ranking from lignite to bituminous) caused by water adsorption is linearly proportional to concentration of water adsorbed,[6,7] we assume that the volumetric swelling strain (e_v^{eq}) developed in coal when water adsorbs is proportional to the adsorbed concentration of water vapour C (mol/kg$_{coal}$) and to the volumetric swelling V_0 produced by sorption of 1 mole of water molecules, with V_0 being indistinguishable for primary and secondary adsorption in cases where both occur. For single layer adsorption (primary adsorption), this assumption can be expressed as $e_v^{eq} = C\rho V_0$.[3,27] For multiple layer adsorption (primary plus secondary adsorption), it becomes $e_v^{eq} = \rho(C_1 V_{01} + C_2 V_{02})$, where the subscript 1 denotes primary adsorption and 2 denotes secondary adsorption, and where $V_{01} = V_{02}$.

2.2. Cases considered and models

In the following, we consider three possible mechanisms responsible for swelling of coal matrix material due to water adsorption, which we will refer to as Mechanisms 1–3. These form the basis for the development of three corresponding models for coupled stress–strain–sorption behaviour, identified as Models 1–3. The details of model derivation can be found in Appendix A. Note here that the effects of stress on adsorption by Mechanism I has already been explored by Hol et al.[3] and by Liu et al.,[13] assuming that general states of stress are supported by the coal matrix material. These authors arrived at general stress–strain–sorption relations for monolayer adsorption of any sorbate species. To date, however, the Dent and the DW models have only been developed and applied for describing water adsorption by unstressed coal,

i.e. for describing sorbed water concentration versus RH or relative pressure in the case of unstressed coal.

Mechanism I: In this case, we assume that only primary adsorption (i.e. monolayer adsorption) occurs inside coal matrix material. This means that the swelling of coal matrix material by Mechanism I is controlled by monolayer adsorption of water molecules in the primary sites. Here, $e_v^{eq} = C\rho V_0$, where C represents the concentration of the first layer of water molecules. Following Hol et al.[3] and Liu et al.,[13] we obtain the corresponding Model 1 for monolayer adsorption induced swelling strain (ε_{ij}^{eq}) by stressed matrix material, which may be formulated as:

$$\varepsilon_{ij}^{eq} = \frac{A_{ij} + \delta_{ij}}{3} e_v^{ads} = \frac{A_{ij} + \delta_{ij}}{3} C\rho V_0 \tag{1a}$$

$$\text{or} \quad \varepsilon_{ij}^{eq} = \frac{A_{ij} + \delta_{ij}}{3} \rho V_0 C_s \frac{a_g K^0 E(\sigma_{ij}, P_0)}{1 + a_g K^0 E(\sigma_{ij}, P_0)} \tag{1b}$$

K^0 (see Appendix A.1 for the expression) is the equilibrium constant for the sorption reaction, which depends solely on temperature. The effect of applied stress on adsorbed concentration and the associated swelling embedded in the occupancy reduction term $E(\sigma_{ij}, P_0) = \exp(\frac{-(\overline{\sigma} - P_0)V_0}{RT}) \exp(\frac{-\sigma'_{ij} A_{ij} V_0}{3RT})$ forms the physical basis for the models developed in this paper for swelling of stressed coal matrix material upon adsorption of water. A_{ij} is a second rank tensor representing the swelling strain anisotropy (see details in Liu et al.[13]), δ_{ij} is Kronecker delta, and R is the gas constant. The term $(\overline{\sigma} + \frac{1}{3}\sigma'_{ij} A_{ij} - P_0) V_0$ represents the stress–strain work done on the surroundings as coal swells against the stress σ_{ij} in excess of the reference pressure of P_0, i.e. $(\sigma_{ij} - P_0\delta_{ij})$.

Mechanism II: Here, swelling of coal matrix material is contributed to by all adsorbed water molecules, and adsorption of water is assumed to involve multiple layer adsorption. In this case, we assume that the total concentration of adsorbed water molecules is described by the widely accepted multiple layer model proposed by Dent.[35] Dent[35] treated the first adsorbed layer of water molecules as primary adsorption, and all subsequent layers as secondary adsorption. Dent further assumed that thermodynamic properties of water adsorbed in the various secondary layers (second, third, fourth and so on) are identical, but different from the properties of the water adsorbed in the primary layer. In line with our assumption above that V_0 is the same for all adsorbed water molecules, to obtain swelling strain from the Dent model for water adsorption, we can write $e_v^{eq} = \rho V_0(C_1 + C_2)$, where C_1 and C_2 represent the concentration of water molecules associated with primary adsorption and secondary adsorption. The Dent-based swelling model (Model 2) may therefore be written as

$$e_v^{eq} = \rho V_0 C_s$$
$$\times \left\{ \begin{array}{l} \dfrac{K_1 E(\sigma_{ij}, P_0)a_g}{1 - K_2 E(\sigma_{ij}, P_0)a_g + K_1 E(\sigma_{ij}, P_0)a_g} \\ + \dfrac{K_1 K_2 E^2(\sigma_{ij}, P_0)a_g^2}{[1 - K_2 E(\sigma_{ij}, P_0)a_g][1 - K_2 E(\sigma_{ij}, P_0)a_g + K_1 E(\sigma_{ij}, P_0)a_g]} \end{array} \right\} \tag{2a}$$

$$\varepsilon_{ij}^{eq} = \frac{A_{ij} + \delta_{ij}}{3} \rho V_0 C_s$$
$$\times \left\{ \begin{array}{l} \dfrac{K_1 E(\sigma_{ij}, P_0)a_g}{1 - K_2 E(\sigma_{ij}, P_0)a_g + K_1 E(\sigma_{ij}, P_0)a_g} \\ + \dfrac{K_1 K_2 E^2(\sigma_{ij}, P_0)a_g^2}{[1 - K_2 E(\sigma_{ij}, P_0)a_g][1 - K_2 E(\sigma_{ij}, P_0)a_g + K_1 E(\sigma_{ij}, P_0)a_g]} \end{array} \right\} . \tag{2b}$$

Mechanism III: In this case, we again assume that swelling is caused by all the adsorbed water molecules, but that these are distributed between separate mono- and multi-layer adsorption

sites. Sorption by this mechanism is described by the widely used D'Arcy and Watt model[36] for water sorption by coal. In the D'Arcy and Watt (DW) model, the monolayer adsorption sites are considered to be the primary adsorption sites while multilayer adsorption sites are the secondary adsorption sites.[20,21,37] In applying this model, we again assume that V_0 is the same for all adsorbed water molecules, regardless of adsorption site type, so that $e_v^{eq} = \rho V_0(C_1 + C_2)$, where C_1 and C_2 represent the concentration of water molecules associated with the primary (monolayer) adsorption sites and the secondary (multilayer) adsorption sites. The formulations for Model 3 (DW-based swelling model) may arrive at

$$e_v^{eq} = \rho V_0 \left\{ \frac{C_{s1} K_1 E(\sigma_{ij}, P_0)a_g}{1 + K_1 E(\sigma_{ij}, P_0)a_g} + \frac{C_{s2} K_2 E(\sigma_{ij}, P_0)a_g}{1 - K_2 E(\sigma_{ij}, P_0)a_g} \right\} \tag{3a}$$

and

$$\varepsilon_{ij}^{eq} = \frac{A_{ij} + \delta_{ij}}{3} \rho V_0 \left\{ \frac{C_{s1} K_1 E(\sigma_{ij}, P_0)a_g}{1 + K_1 E(\sigma_{ij}, P_0)a_g} + \frac{C_{s2} K_2 E(\sigma_{ij}, P_0)a_g}{1 - K_2 E(\sigma_{ij}, P_0)a_g} \right\} . \tag{3b}$$

2.3. Swelling under stressed versus unstressed conditions: A comparison of model predictions

All three models expressed in Eqs. (1)–(3) demonstrate that swelling of coal matrix material upon adsorption of water at a reference fluid pressure of $P_0 = 0.1$ MPa under an applied stress state $\sigma_{ij} > P_0\delta_{ij}$ or under a hydrostatic stress state $\sigma > P_0$, is clearly lower than that under conditions, where $\sigma_{ij} = P_0\delta_{ij}$. The same applies for any fluid pressure P ($\sigma = P$), of course. The effect is due to the influence of the term $E(\sigma_{ij}, P_0)$, i.e. to the stress–strain work done in association with sorption-induced swelling against the positive stress $\overline{\sigma}$ in excess of reference pressure of P_0, i.e. $(\overline{\sigma} - P_0)$, and against the deviatoric stress σ'_{ij} under stressed conditions, which reduce the adsorbed concentration of water by coal matrix. Our Models 1–3 therefore all predict that the higher the applied stress in excess of P_0, the lower the sorbed water content at equilibrium and the lower the resulting swelling strain. It is also clear from all models that at a given applied stress state, the magnitude of the effect of the applied stress in reducing sorbed concentration and swelling depends on V_0. This crucial term, V_0, i.e. the volumetric swelling that occurs per mole of adsorbed water, can be derived from sorption-induced swelling experiments on either stressed or unstressed coal, via Eq. (3a), and typically lies in the range 4 to 13×10^{-6} m³/mol.[6,7]

3. Experiments

As shown above, our models (i.e. Eqs. (1)–(3)) predict that an (effective) stress applied in excess of the reference pressure P_0 reduces swelling of coal matrix upon adsorption of water. In the following, we test the validity of our models by experimentally investigating the swelling response of coal samples upon adsorption of water at different applied stress states, using a uniaxial compaction/compression apparatus. Experiments were performed on a solid disc and pre-compacted powdered coal samples at a constant temperature of 40 °C. The mechanical response of the samples, under both vacuum dry (i.e. 0% relative humidity) and wet (i.e. 100% relative humidity) conditions was first determined by loading axially in a stepwise manner. Note that the terms "evacuated state" and "water-exposed state" are used to refer to vacuum dry and wet conditions. We also measured the axial swelling strain response of (vacuum) dry samples to the introduction of distilled water at a fluid pressure of 0.1 MPa, at constant applied stress states.

3.1. Starting materials and sample preparation

The samples used in all experiments were prepared from high volatile bituminous coal which was obtained from the Brzeszcze mine (seam 364) in the Upper Silesian Basin of Poland. The Brzeszcze coal has a vitrinite reflectance of 0.77 ± 0.05%, and contains 74.14% carbon, 5.27% hydrogen, 1.44% nitrogen, 0.70% sulphur and 18.45% oxygen.[16] Specifically, the coal samples used in this study contain 2.93% moisture content, and 5.16% ash content. Experiments were conducted on both a single 1 mm thick solid disc and 10 pre-compacted powdered samples (grain size of 180–212 μm). The samples were tested in the titanium sample vessel shown in Fig. 1(a) (inner diameter 12.18 mm, outer diameter 19.1 mm[38]). The titanium vessel, plus sample, porous plate (<100 μm) and titanium pistons will be referred to henceforth as the sample assembly. This was assembled and transferred to the main experimental apparatus in order to execute the experiments.

3.1.1. Coal disc sample

After identifying the bedding plane of a ~10 cm slab, several cores with a diameter of 11.8 mm and length of ~5 mm were drilled along the direction perpendicular to the bedding plane using a water-cooled pillar drill. Subsequently, the 5 mm long cylinders were accurately sectioned into 1 mm thick discs. Both ends of the discs were ground flat. This was done by Glass Workshop of Utrecht University. One optically (by means of optical microscope with a magnification of *5) cleat-free disc was chosen for the present experiments. The sample was pre-dried in an oven at 40 °C under vacuum for ~3 days. The mass and dimensions of the sample were then measured, immediately prior to experimentation, and average values were recorded (Table 1). Porosity of the sample P_disc_5 was estimated, taking the average density obtained from two 1 mm sized cube (same coal material with less micropores), as used by Liu et al.[10] as the reference density of matrix material (1320 ± 34 kg/m³).

Note here that the diameter of disc sample is 11.80 mm, which is less than the inner diameter 12.18 mm of the titanium sample vessel. The space between the disc and the vessel wall was accordingly 0.38 mm, which is equivalent to a 3.2% strain of the disc sample in the radial direction. This means there is enough space for the disc to freely expand radially, without touching the vessel wall, in response to either elastic deformation (<1.5%) or sorption induced swelling (<0.5%). The free space around the sample rim means that water will diffuse into the sample from both the top and rim of the sample, though with different characteristic times due to differing length scale and likely anisotropic diffusion coefficients in the radial versus axial directions. Also note that for such a short cylinder, there would be significant shear stresses on the endcaps of the disc sample upon radially expansion. The term "applied axial stress" used in this paper refers to the stress applied by the uniaxial compression apparatus.

3.1.2. Powdered coal samples

The grain size of the powdered coal samples used in the present experiments was 180–212 μm. This grain size fraction was prepared by crushing and sieving the remaining part of the slab used for preparing the solid coal disc sample. Samples weighting 0.15–0.2 grams were used for each experiment on coal powder, pre-drying in an oven at 40 °C under a vacuum condition for 1 day. In setting up each experiment, the sample powder was distributed evenly in the titanium vessel and a flat, disc-shaped sample was pre-formed by manually compressing it by hand-loading the upper and lower titanium pistons. The thickness of the disc-shape powdered sample measured after the experiments was taken as the dimensions used in all strain and initial dimension calculations and ranged from 1.2–1.9 mm (Table 1). The estimated porosity of the pre-compacted samples lay in the range of 23%–28%.

Note here that the pre-compacted powders were only able to expand in the axial direction, because expansion in radial direction was constrained by the titanium sample vessel. This means the axial swelling strain measured in the experiments on powdered samples represents both the axial and the volumetric swelling strain of the samples.

3.2. Apparatus

The experimental setup shown in Fig. 1(b) consists of a uni-axial, oedometer-type (i.e. one dimensional) compaction vessel, constructed of Remanit 4122 stainless steel, mounted in an Instron 8562 servo-controlled loading frame to apply axial load.[16] In this study, the Instron loading frame was operated in load control mode. The sample assembly (Fig. 1(a)) was axially loaded, within the Remanit vessel via two Remanit pistons (diameter 19 mm) sealed against the Remanit compaction vessel using Viton o-rings. Applied axial load was measured external to the compaction vessel using a 100 kN capacity Instron loadcell, which allows load control to within ±0.0023 kN. Axial displacement of the upper piston relative to the Remanit vessel top (i.e. axial sample deformation) was measured using a high precision LVDT (measuring stroke ±1 mm, accuracy better than ±0.1 μm). This allowed changes in sample thickness to be measured accurately at any instant, by correcting for piston distortion. The liquid distilled water was introduced into the sample through the inlet in the upper Remanit piston. The pressure of the fluid was measured using a Honeywell pressure transducer.

The temperature of the compaction vessel and sample were controlled at 40 °C (±0.1 °C) in the present experiments by means of an external furnace mounted around in the Remanit compaction vessel. This was regulated by means of a Eurotherm temperature controller, connected to a type K thermocouple located in the external furnace windings. Sample temperature was measured using a second type K thermocouple placed in a small recess in the outer compaction pressure vessel at a distance of ~0.5 mm from the titanium sample vessel. To minimize distortion of the Instron loading frame caused by temperature fluctuations, a 1.5 m³ foam-polystyrene box was constructed around the setup to control the air temperature in the box at 30 ± 0.2 °C, using an internal lamp, fan and CAL 9900 PID-controller[27] (see Fig. 1(b)).

3.3. Testing procedures

Compression tests were performed in stepwise loading mode on both the solid disc sample P_disc_5 and one powdered sample (Powder_1) to determine the mechanical response of the samples in both the evacuated and water-exposed states. Swelling tests were then performed on both P_disc_5 and ten powdered samples (Powder_1–10) to measure the time-dependent swelling behaviour of the samples during exposure to distilled liquid water (at 0.1 MPa) at fixed applied stress. Note that in all experiments, we assumed an apparent equilibrium state when no change in displacement, i.e. in LVDT (<0.2 μm) signal could be identified within a period of 2 h. Note that calibrations have been performed before experimental tests and details can be found in Appendix B.

3.3.1. Compression tests under evacuated vs. water-exposed conditions

These experiments, performed on samples P_disc_5 and Powder_1, involved four sequential stages:

(1) Pre-compaction and cyclic loading under vacuum. To minimize permanent deformation and remove the residual water content of the coal samples, both the fresh P_disc_5 and Powder_1 were pre-compacted at 13 kN under vacuum (applied via Valves A

Table 1
Dimensions, mass and porosity of the Brzeszcze 364 coal samples (i.e. both the disc and powdered coal samples) used in this study. The listed dimensions were used for all strain and porosity (change) calculations. Note that the listed dimensions obtained for Sample P_disc_5 were measured before the experiments. Any change after experiments was below measurement resolution (digital calliper). The dimensions listed for the powdered samples were measured after the experiments. The types of experiment (Exp) performed on each sample are also indicated. Porosity values quoted are total porosity including matrix porosity and, in the case of the powdered samples, intergranular porosity.

| Sample	Initial sample mass (g)	Sample thickness l (mm)	Sample diameter d (mm)	Porosity (%)	Exp.
P_disc_5	0.13852	1.000	11.80	3.99	Compression/Swelling
Powder_1	0.20203	1.740	12.18	24.47	Compression/Swelling (25.6MPa)
Powder_2	0.19927	1.735	12.18	25.29	Swelling (43.2MPa)
Powder_3	0.21033	1.800	12.18	23.99	Swelling (60.5MPa)
Powder_4	0.19679	1.700	12.18	24.70	Swelling (77.8MPa)
Powder_5	0.15722	1.420	12.18	27.98	Swelling (25.6MPa)
Powder_6	0.153747	1.340	12.18	25.36	Swelling (43.2MPa)
Powder_7	0.14404	1.240	12.18	24.43	Swelling (60.5MPa)
Powder_8	0.204078	1.720	12.18	22.82	Swelling (77.8MPa)
Powder_9	0.22370	1.940	12.18	24.99	Swelling (60.5MPa)
Powder_10	0.22318	1.910	12.18	23.99	Swelling (60.5MPa)
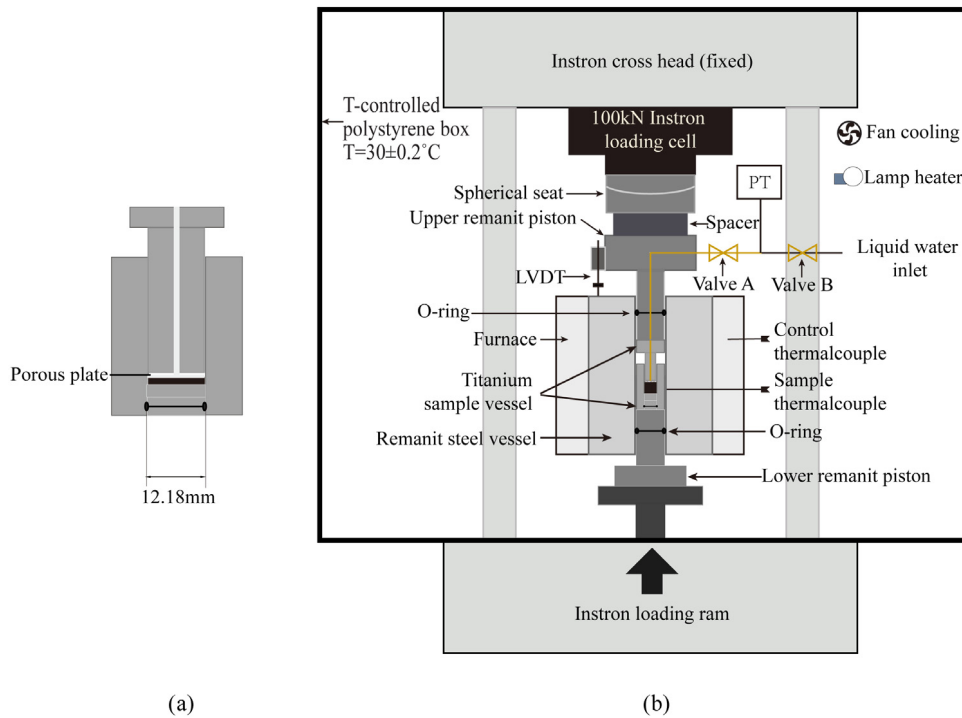
Fig. 1. Schematic diagram of the present 1-D loading system. (a) Sample assembly consisting of titanium sample vessel, piston, porous plate, and sample. (b) Compaction cell constructed of Remanit steel located in an Instron loading frame operated in a load control mode. The sample assembly was located inside the bottom of the Remanit steel vessel, in series with the loading piston. In wet experiments, liquid distilled water was introduced into the sample through the inlet in the upper piston. An external LVDT mounted on the upper Remanit piston was used to measure the deformation of the sample in the axial direction, correcting for apparatus distortion. The temperature of the vessel and sample were controlled at a temperature of 40 °C (±0.1 °C). A heated polystyrene box enclosed the full setup, maintaining a constant air temperature in the box of 30 °C (±0.2 °C) and thus avoiding effects of thermal expansion of the Instron and other components, caused by temperature fluctuations.

and B in Fig. 1(b)). This load condition is equivalent to 118.9 MPa for P_disc_5 and 111.6 MPa for Powder_1. Pre-compaction was carried out for ~20 h for P_disc_5 and ~40 h Powder_1. The samples were then unloaded to the target starting load of the experiments, i.e. to 9.15 MPa for P_disc_5 and to 25.95 MPa for Powder_1. A slow expansion of the sample was subsequently observed, apparently caused by the release of elastic energy stored in the coal samples during pre-compaction via time dependent (creep) processes. After re-equilibration at the target load conditions, load cycling was conducted several times, in the range of ~9 to ~100 MPa at a rate of 0.1 MPa/s, to further minimize permanent deformation effects during subsequent testing.

(2) Stepwise compression tests in the evacuated state. To determine the mechanical response of the samples due to changes in applied stress states, we performed axial compression experiments under vacuum (i.e. 0% relative humidity), by applying the following upward loading steps. The stresses applied to P_disc_5 were 9.15, 27.45, 45.74, 64.04, 82.34, and 100.64 MPa, while for Powder_1 the applied stresses were 25.93, 43.22, 60.50, 77.79, and 95.08 MPa. Re-equilibration time with respect to deformation occurring after each stress step was around 5 min for P_disc_5, and around 15 min for Powder_1. Note that to minimize the thermodynamic stress–strain–sorption effects potentially occurred for wet samples[3,13,16] during loading, the loading rate employed for compression tests was rapid and constant at 0.2 kN/s, which is equivalent to ~1.83 MPa/s for P_disc_5, and ~1.73 MPa/s for Powder_1. This loading rate allowed each loading step in the compression experiments to be completed within 10 s. Compression testing was terminated by unloading the samples from the maximum compressive stress applied, back to the starting load and reaching equilibrium at that stress (9.15 MPa for P_disc_5 and 25.93 MPa for Powder_1).

(3) Equilibration with distilled liquid water (water-exposed state). After equilibration at the starting stress (of 9.15 MPa applied to P_disc_5 and of 25.93 MPa to Powder_1) under vacuum (evacuation of the samples via Valves A and B, Fig. 1(b)), Valve A was closed and degassed distilled (liquid) water was introduced into the pipe between Valves A and B in Fig. 1(b). This led to a slight change in LVDT signal due to the temperature fluctuation caused by opening the temperature-controlled box and the cold water injection. After the output signal of the LVDT re-stabilized, i.e. the temperature of both the box and water were re-stable at 30 °C, the Valve A was re-opened to allow liquid water to enter into the sample. Initial equilibration took around 24 h for P_disc_5 at an initial stress state of 9.15 MPa and for Powder_1 at an initial stress state of 25.93 MPa.

(4) Stepwise compression tests in the water-exposed state. Once the samples had approached equilibrium with liquid water at the above initial applied stress state, the applied stress was increased in steps, allowing apparent equilibrium to be reached or at least approached after each increment. Two loading–unloading runs or cycles were performed on P_disc_5, while a single cycle was performed on the pre-compacted Powder_1, following the loading steps described in Stage 2.

3.3.2. Swelling measurements at fixed stress states

In these experiments, we measured the time-dependent swelling strains of P_disc_5 and our ten pre-compacted powdered samples (Powder_1-10) upon introduction of distilled liquid water (at 0.1 MPa) at fixed stress states (Table 1). The stress was kept constant throughout each experiment but varied from test to test. In all swelling experiments, the sample was first pre-compacted and cyclically loaded, under vacuum, following the above procedure (point 1). Water was then introduced, again following the above procedure (point 3). We performed 5 independent swelling experiments on P_disc_5 at fixed stress states of 27.45, 45.74, 64.04, 82.34, and 100.64 MPa. The ten experiments on pre-compacted powdered samples (Table 1) were performed at stress states of 25.93, 43.22, and 77.79 MPa (two experiments per stress), and at stress states of 60.50 MPa (four experiments).

3.4. Data acquisition and processing

The temperature (°C) of the samples, the polystyrene box, and the Instron, the output signals of the external LVDT (mm), and the Instron load (kN) and position (mm), were recorded using a National Instrument, 16-channel DAOPad-6015 A/D converter and VI-logger data acquisition system, employing a sampling rate of 0.2 Hz.

3.4.1. Compression data processing

The axial (compressive) strains of the samples occurring under both evacuated and water-exposed states upon changes in applied stress states were obtained by correcting for the distortion of the apparatus as described above. Note here that zero axial strain of the samples refers to the initial stress state of 9.2 MPa for P_disc_5 and 25.9 MPa for Powder_1, and compressive stress and strain are taken as positive.

For the water-exposed state, deformation of the samples upon changes in applied stress states includes rapid deformation (i.e. essentially time-independent deformation) and slow time-dependent deformation. The time-dependent axial compressive strain (e^i) of the sample at stress level of i was calculated by subtracting the rapid deformation. From the compression tests performed in the evacuated state, equilibration of the rapid deformation associated with elastic deformation took 5 min for P_disc_5 and 15 min for the pre-compacted sample Powder_1, probably reflecting thermal effects and poroelastic effects upon pore pressure

diffusion.[39] We therefore calculated the time-dependent compressive strain attained at apparent equilibrium for the wet samples, at stress level i, by subtracting the rapid deformation that occurred within the first 10–20 min at the ith stress state, assuming that this is purely caused by thermo-elastic effects.

3.4.2. Swelling data processing

The total axial swelling strain e^{total} (swelling measured as positive) measured in the swelling tests includes rapid deformation (e^{dis}, see 3.4.2) of the apparatus due to introduction of 0.1 MPa liquid water, rapid elastic deformation (e^{el}) of the sample due to the change in stress state caused by introduction of 0.1 MPa liquid water, and slow time-dependent swelling strain ($e(t)$) of the sample. The elastic deformation of the sample was estimated using the sample compliance obtained from the compression tests in the evacuated state. This elastic deformation amounted to a $\sim$0.06 μm displacement for P_disc_5 and a $\sim$0.1 μm displacement for the powdered samples, which were small enough to be neglected.

In the case of P_disc_5, time-dependent swelling strain ($e(t)$) of the sample was obtained from the total swelling strain (e^{total}) by subtracting the distortion of the apparatus (e^{dis}), i.e. $e(t) = e^{total} - e^{dis}$. Since e^{dis} occurred immediately after the introduction of water into the sample, the time-dependent axial swelling strain (positive) of the sample (%) can be calculated using the expression $e(t) = \frac{L(t) - L_0}{l}$. Here, L_0 (mm) represents the output signal of the LVDT at the instant immediately after the rapid change in LVDT signal, while $L(t)$ (mm) represents the LVDT signal after t seconds of subsequent time-dependent swelling. The quantity l (mm) represents the initial thickness of the sample. The average value of $e(t)$ over the final 2 h was taken as the equilibrium axial swelling strain (e^{eq}) of the sample during exposure to water.

In the case of the powdered samples, the time-dependent swelling strain measured upon introducing water is assumed to equal the total swelling strain measured, as the elastic distortion of the apparatus and sample are small enough to be neglected.

4. Results

4.1. Compression test data: P_disc_5 vs. pre-compacted Powder_1

Compression data for P_disc_5 and the pre-compacted powdered sample Powder_1, as obtained under both evacuated and initial water-exposed states, are shown in Figs. 2 and 3, respectively. Compressive axial strain (%) and the applied axial stress (MPa) are measured as positive. Axial strain was arbitrarily set to zero at the starting stress state of each loading run, i.e. at the initial applied stress of 9.15 MPa for P_disc_5 and of 25.93 MPa for Powder_1.

In the case of the sample P_disc_5 loaded under vacuum (i.e. in the evacuated state), raw LVDT (mm) and applied load (kN) data are plotted as a function of time (min) in Fig. 2(a). The corresponding stress–strain data (full set) are plotted in Fig. 2(b). Fig. 2(a) shows that strain "equilibration" following each applied load increment typically took about 5 min, reflecting instantaneous elastic deformation during active loading followed by minor (reversible) time-dependent deformation presumably due to thermal effects. Total test duration was about 55 min. The strain–stress data shown in Fig. 2(b) illustrate non-linear (load-stiffening) mechanical behaviour of the sample that is closely recoverable but with marked hysteresis. For the water-exposed sample P_disc_5, the raw LVDT (mm) and applied load data are plotted as a function of time (hours) in Fig. 2(c). The corresponding stress–strain data (full set) are plotted in Fig. 2(d). Fig. 2(c) shows that apparent equilibrium at each applied load took 13–34 h, during which time significant time-dependent strains were accumulated after active loading. The total test duration was $\sim$240 h. Similar non-linear (load-stiffening) stress–strain behaviour was observed, as during
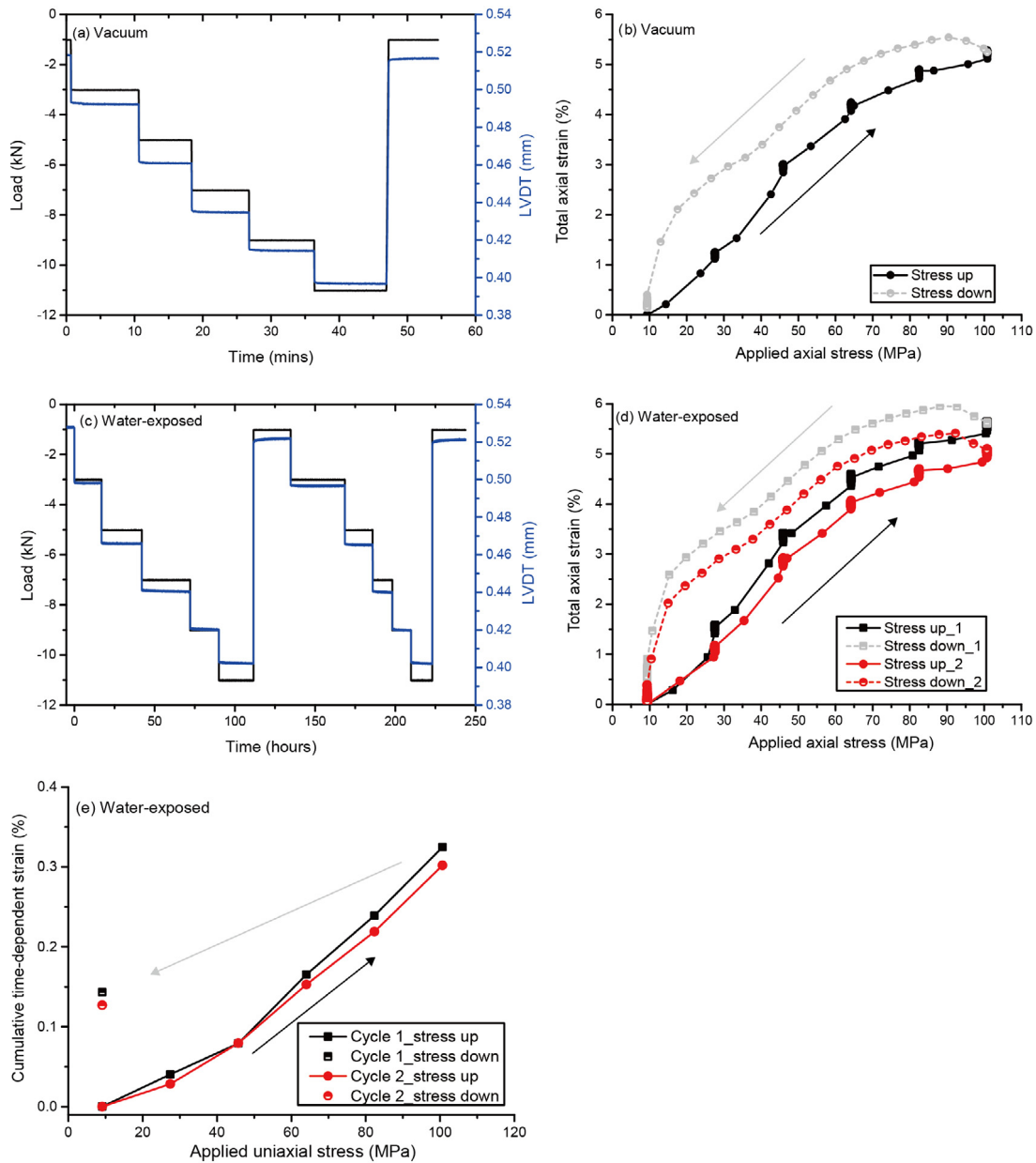
Fig. 2. Compression test data for sample P_disc_5. (a) Raw LVDT (mm) and applied load (kN) data are plotted as a function of time in the evacuated state. (b) The corresponding total axial strain (%) versus applied axial stress (MPa) data in the evacuated state. (c) Raw LVDT (mm) and applied load (kN) data are plotted as a function of time in the water-exposed state. (d) The corresponding total axial strain (%) versus applied axial stress (MPa) data in the water-exposed state. (e) The cumulative time-dependent (compressive) strains for the water-exposed sample against the applied axial stress. Time dependent compressive strain during each period of constant stress was obtained from apparent equilibrium strain subtracting rapid deformation occurred within first 10 min after a change in applied axial stress. Note that "stress up" refers to upward loading, while "stress down" refers to downward part of cycle.

loading under vacuum (compare Fig. 2(d) and (b)). However, as seen in Fig. 2(d), a total permanent strain of 0.55% remained after the first loading cycle, while closely recoverable deformation occurred in the second loading cycle. Marked hysteresis was observed in both loading cycles. The cumulative, time-dependent strains occurring after 10 min of ceasing active loading (to avoid thermal effects observed in the evacuated state, Fig. 2(a)) are plotted for the water-exposed samples in Fig. 2(e) as a function of the applied axial stress. The total time-dependent deformation accumulated at maximum stress during each up-loading run was ∼0.32% while a small residual time-dependent permanent (hence creep) deformation of ∼0.14% was observed after unloading to, and equilibration at, the initial stress of 9.15 MPa in both loading cycles on the wet disc (Fig. 2(e)). This demonstrates that the time-dependent deformation shown in Fig. 2(e) consists of a reversible

component of time-dependent compressive deformation (∼0.18% strain) plus a time-dependent permanent or creep component (∼0.14% strain). A non-linear relation between cumulative, time-dependent strains and applied axial stress is also visible from Fig. 2(e). When the stress increased from 9.2 MPa to 45.7 MPa, the time-dependent deformation generated at each stress step was ∼0.04%, while it was ∼0.08% when the stress was increased from 45.7 MPa to 100.6 MPa.

Similar behaviour to that reported above for sample P_disc_5 was observed for the pre-compacted coal sample Powder_1, in the both evacuated and water-exposed states (see Fig. 3). However, there are also some important differences in behaviour. In the evacuated condition, sample Powder_1 showed larger time-dependent deformations in the approach to equilibrium strain after each loading increment, with equilibration to a plateau strain
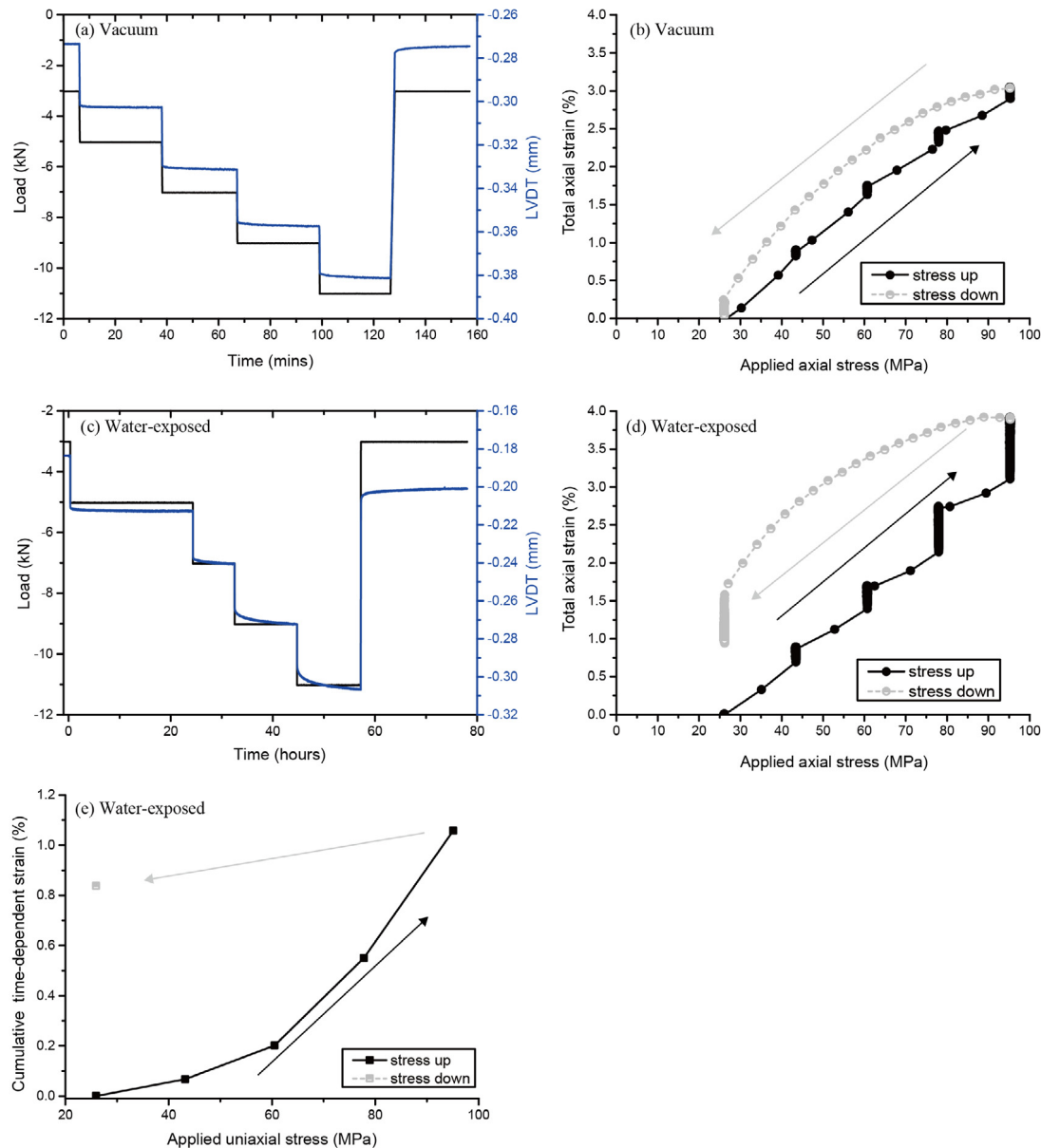
Fig. 3. Compression test data for the pre-compacted powdered sample Powder_1. (a) Raw LVDT (mm) and applied load (kN) data are plotted as a function of time in the evacuated state. (b) The corresponding total axial strain (%) versus applied axial stress (MPa) data in the evacuated state. (c) Raw LVDT (mm) and applied load (kN) data are plotted as a function of time in the water-exposed state. (d) The corresponding total axial strain (%) versus applied axial stress (MPa) data in the water-exposed state. (e) The cumulative time-dependent compressive strains for the water-exposed sample against the applied axial stress. Time-dependent compressive strain during each period of constant stress was obtained from apparent equilibrium strain subtracting rapid deformation occurred within first 20 min after a change in applied axial stress. Note that "stress up" refers to upward loading, while "stress down" refers to downward part of cycle.

taking around 15 min per step (see Fig. 3(a)). The duration of the single run performed under vacuum was around 160 min. The full set of strain–stress data shown in Fig. 3(b) illustrate near-linear (thermo-elastic) behaviour of the sample under vacuum, this behaviour being closely recoverable but with clear hysteresis.

For the water-exposed state, the data obtained for sample Powder_1 show that apparent equilibrium took 8–22 h after each change in applied load (Fig. 3(c)). The single load cycle performed took ~80 h in total. Active loading during upward stress stepping yielded relatively linear stress–strain behaviour as shown in the full set of strain–strain curve presented in Fig. 3(d). However, large amounts of time-dependent deformation occurred in the water-exposed state at each stress state applied, typically around 0.2 to 0.8% strain per stress level (see vertical data segments in Fig. 3(d)). Upon unloading from the maximum stress applied (95.05 MPa) to the initial applied stress of 25.93 MPa, irreversible behaviour with

a total permanent strain of ~0.9% was observed after equilibration (Fig. 3(d)). Cumulative, time-dependent strains versus applied axial stress data are shown in Fig. 3(e). This shows that the higher the stress state, the more and the faster time-dependent deformation occurred. A total time-dependent compressive strain of ~1.09% was observed after equilibration at maximum applied stress, of which ~0.84% strain was permanent (the strain after equilibration upon unloading to the initial stress of 25.93 MPa) and ~0.25% was reversible (Fig. 3(e)).

4.2. Swelling data: P_disc_5 vs. pre-compacted powdered samples

The axial swelling strain data obtained for sample P_disc_5 and the full suite of pre-compacted powdered samples, upon introduction of water into the evacuated samples at fixed stress
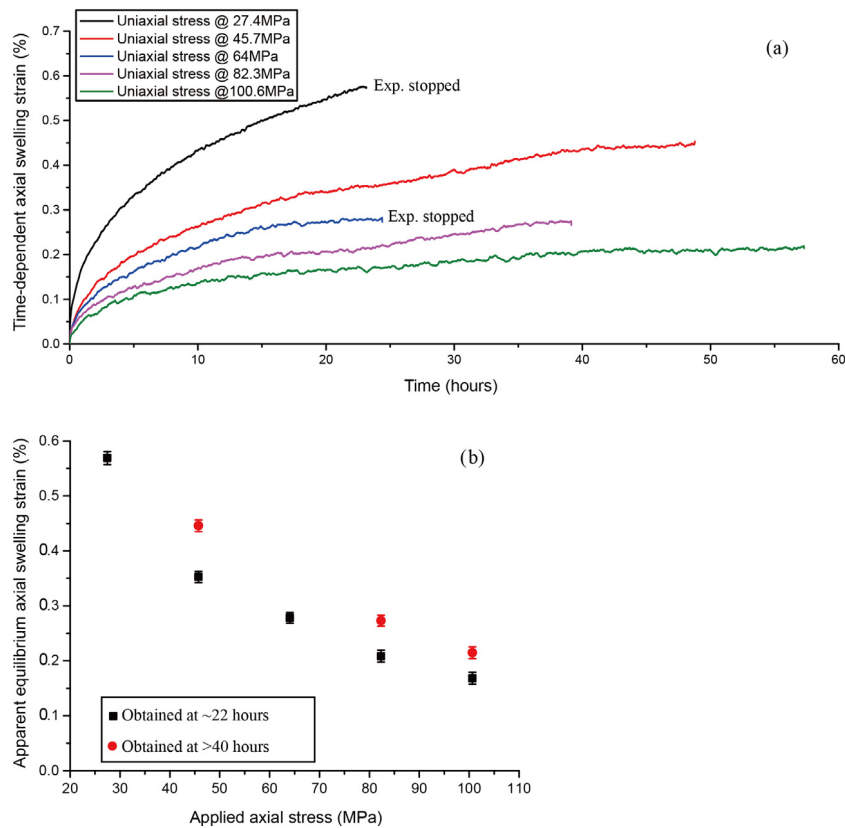
Fig. 4. Axial swelling strain (%) attained for P_disc_5 in the direction perpendicular to bedding during exposure to distilled liquid water at an absolute fluid pressure of 0.1 MPa (1 atm). (a) Axial swelling strain versus time, corrected for apparatus distortion and elastic deformation of the sample due to injection of 0.1 MPa liquid water into the evacuated sample. (b) Axial swelling strain, measured in the approach to equilibrium at 22 and 40 h elapsed time, versus axial stress applied by the uniaxial compression apparatus.

states, are shown in Figs. 4 and 5, respectively. Note here that axial swelling strains are measured positive, as are the applied compressive stresses. Broadly speaking, all samples (P_disc_5 and samples Powder_1-10, Figs. 4 and 5), expanded in a time-dependent manner, after introduction of liquid water, until an asymptotic or apparent equilibrium strain value was reached (Figs. 4(a) and 5(a)). Importantly, the swelling strains attained at apparent equilibrium decreased with increasing applied stress states. In the case of P_disc_5, axial swelling strain gradually developed with time after introducing water via Valve A (Fig. 1), approaching a nearly constant or apparent equilibrium strain after 22–40 h in most cases (Fig. 4(a)). Swelling strains attained at ∼22 h for all experiments performed on P_disc_5 are presented against applied axial stress in Fig. 4(b) (black dots). These data show that the axial swelling strains obtained normal to bedding, as equilibrium was approached, decreased non-linearly from 0.569% to 0.168% as the applied axial stress increased from 27.4 MPa to 100.6 MPa. Swelling strains attained (at >40 h) in the three experiments that ran for 40 h or more are also plotted in Fig. 4(b) (red dots). These decreased with increasing applied axial stress following a similar trend, though the absolute strains are slightly higher than that attained at ∼22 h at the same applied axial stress, because equilibrium was more closely approached at 40 h.

In the case of the pre-compacted powdered samples, axial swelling strain development with time is shown in Fig. 5(a). The origin of the time axis in Fig. 5(a) refers to the moment that we opened the Valve B, shown in Fig. 1, to let liquid water enter the pipe section A–B, keeping Valve A closed in an attempt to maintain the sample in the vacuum dry state. The zero point on the strain axis in Fig. 5(a) refers to the LVDT output or strain state just prior opening Valve A. From this figure, it is clear that in

the seven tests performed on samples Powder_3 and Powder_5-10, large time-dependent expansions were observed after opening Valve B but before opening Valve A (i.e. before the liquid water entered the sample). These time-dependent expansions approached asymptotic (or apparent equilibrium) swelling strains of 0.22–0.93% within a period of 2.5 to 6 h after opening Valve B. This swelling, was presumably caused by adsorption of water vapour that diffused into the samples through Valve A after opening Valve B. However, after water was admitted to the sample by opening Valve A, rapid expansion developed within the first hour in all tests, with the swelling strains attained in this stage reaching more than 95% of the final apparent equilibrium strain measured with respect to the zero point on the strain axis. After this fast expansion, slow expansions were observed at the applied stress states of 25.9 and 43.2 MPa, while slow, time-dependent compaction occurred at 60.5 and 77.8 MPa. The total, near-equilibrium (plateau) swelling strains, averaged over the last two hours of each experiment, are plotted versus the applied uniaxial stress states in Fig. 5(b). Note that these swelling strain data include the apparent equilibrium swelling strain caused by water vapour entering via Valve A before liquid water was admitted to the samples, plus the apparent equilibrium swelling strain caused by adding the liquid water. The results show that the total equilibrium swelling strain attained at apparent equilibrium decreased more or less linearly, from 1.889% strain to 0.615% strain, when the applied uniaxial stress state increased from 25.9 to 77.8 MPa (Fig. 5(b)).

4.3. Swelling kinetics data

Following the standard treatment employed in presenting sorption and swelling data as a function of time to investigate process
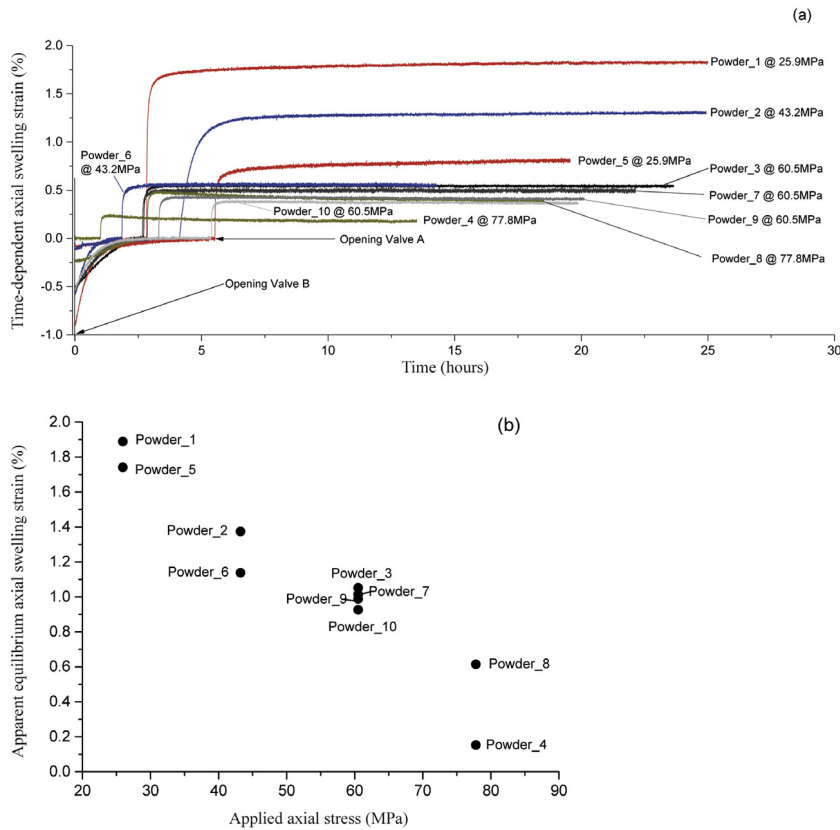
Fig. 5. Axial swelling strain (%) attained for all pre-compacted powdered samples during exposure to distilled liquid water at an absolute fluid pressure of 0.1 MPa. (a) Axial swelling strain versus time. The origin of the time axis refers to the moment that we opened the Valve B (Fig. 1(b)) to let liquid water enter pipe segment A–B in Fig. 1, keeping Valve A closed in an attempt to maintain the sample in the vacuum dry state. The zero strain point on the strain axis refers to the LVDT output or equivalent strain at the moment just prior to admitting liquid water into the sample by opening Valve A. (b) Total axial swelling strains attained at apparent equilibrium versus applied uniaxial stress. The total swelling strain data shown in (b) were obtained by averaging the swelling strain data obtained in the final two hours shown in a, all measured relative to the strain at the first onset of swelling. The swelling strain data in b thus include the apparent equilibrium swelling strain caused by water vapour entering via Valve A before liquid water was admitted to the samples, plus the apparent equilibrium swelling strain caused by adding the liquid water.
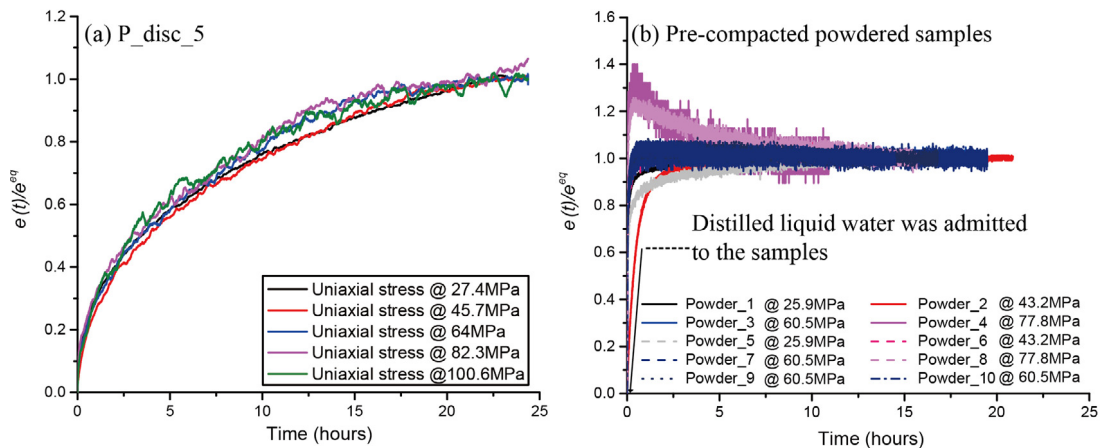

Fig. 6. Normalized swelling strains of samples (expressed as the ratio $e(t)/e^{eq}$) upon adsorption of distilled water at given fixed applied stress states versus time. (a) P_disc_5. (b) Pre-compacted powdered samples after liquid water was admitted to the samples.

kinetics,[18,40–42] normalized swelling strains ($e(t)/e^{eq}$) due to adsorption of distilled water at given fixed applied stress states are plotted in Fig. 6 as a function of time, for all of our samples. Note here that the swelling data for the pre-compacted powdered samples plotted in Fig. 6(b) represent swelling strain data (measured with respect to the zero point on the strain axis in Fig. 5(a)) plotted against elapsed time from the moment at which the distilled (liquid) water was admitted to the samples via Valve A (thus avoiding displaying the rate of swelling that occurred in cases where water

vapour diffused into the samples via Valve A at an earlier stage). It is clear from Fig. 6(a) that swelling rates for P_disc_5 are insensitive to applied stress state. However, from Fig. 6(b), it is evident that the swelling rate of the pre-compacted powdered samples (grain size within 180–212 μm) is much faster than that for P_disc_5 (1 mm disc) at similar applied stresses. Moreover, the effect of applied stress on swelling kinetics of the pre-compacted powdered samples (Fig. 6(b)) is much more complicated than in the case of sample P_disc_5 (Fig. 6(a)), as considerable variability in swelling

behaviour occurred in the swelling experiments due to the complications of water vapour entering some samples before liquid water was admitted, and of some powdered samples showing minor, late stage compaction (see Fig. 5(a)). The effects visible in Fig. 5(a), namely (a) the time-dependent swelling behaviour seen before admitting liquid water into the samples, and (b) the time-dependent compaction behaviour seen at higher stress states after contact with liquid water, strongly influence the swelling rates shown in Fig. 6(b). Note, however, behaviour of Sample Powder_2 at a stress state of 43.2 MPa. In this experiment, there was no time-dependent swelling before the sample was exposed to liquid water, nor did time-dependent compaction occur after liquid water was admitted into the sample (see Fig. 5(a)). This sample shows the slowest swelling rate in Fig. 6(b).

5. Discussion

The swelling data presented above for our coal disc and powdered coal samples have demonstrated that the higher the axial stress applied to the samples, the lower the swelling of coal samples due to adsorption of water after introduction and equilibration at a fixed absolute fluid pressure of 0.1 MPa. This finding is consistent with the model predictions of all of our models for the thermodynamic effect of stress on sorption capacity. However, the stepwise loading tests performed on the water-exposed samples (P_disc_5 and Powder_1) showed the strains achieved at (apparent) equilibrium to consist of a reversible elastic component, a reversible component of time-dependent deformation, plus a permanent component of time-independent deformation (1st run) as well as time-dependent deformation (creep). This means that the reduction in swelling strain observed with increasing applied stress in the swelling tests might be due not only to a stress-related reduction in adsorbed water concentration at equilibrium, but to additional mechanisms allowing both (a) permanent creep, and (b) reversible time-dependent deformation that is independent of reversible sorption and associated time-dependent deformation.

In the following, we will further discuss the mechanisms responsible for the stress-driven reduction in swelling. We start this by comparing our experimental data with predictions made regarding reversible thermodynamic stress–strain–sorption effects using the three models presented in Section 2, with the aim of explaining departures from this in terms of other possible processes. We go on to discuss the differences in behaviour observed between the disc and powered samples, and the difference in mechanical response of the samples seen between dry and wet states. Finally, we consider the likely implications of our findings for (E)CBM recovery.

5.1. Mechanisms responsible for the stress-driven reduction in swelling

5.1.1. Thermodynamic effect of applied stress on water adsorption: comparison with model predictions

To determine whether the stress-driven reduction in swelling that we measured in the swelling experiments is explained by stress-driven reduction in water adsorption capacity, versus other processes such as creep, we compare our swelling data for both disc and powdered samples with the predictions made by the three models derived in Section 2. To predict the magnitude of swelling strain caused by adsorption of water using our models (Eqs. (3), (4), (7) and (10)), we need to know the stress states, the swelling strain anisotropy tensor A_{ij}, the volumetric swelling per mole of adsorbed water molecules V_0, the equilibrium constants (K^0, K_1, K_2) and adsorption site concentrations (C_s, C_{s1}, C_{s2}) for both the disc and powdered samples.

We consider two end-member stress states as potentially applying to sample P_disc_5 (see 5.2), i.e. uniaxial stress $\sigma_{ij} = \begin{pmatrix} \sigma & 0 & 0 \\ 0 & 0 & 0 \\ 0 & 0 & 0 \end{pmatrix}$ (laterally unconfined case, taking the compression direction and bedding plane normal to be the x_1 direction) and hydrostatic stress $\sigma_{ij} = \sigma \delta_{ij}$ (laterally confined and assuming constant sample volume). These correspond respectively to the minimum and maximum possible effects that the applied axial stress can exert on the sorption capacity of Sample P_disc_5, according to the models we have developed. For the pre-compacted powdered samples, which were constrained laterally from the outset, we assume that the stress state was approximately hydrostatic, so that $\sigma_{ij} = \sigma \delta_{ij}$. Also assuming that the pre-compacted samples were mechanically more or less isotropic, this assumed hydrostatic stress state corresponds to the maximum impact that the applied stress can have on reducing water adsorption capacity due to the thermodynamic stress–strain–sorption effects captured in our models.

Regarding A_{ij}, the swelling strain anisotropy tensor, for P_disc_5, this was assumed to be given by $A_{ij} = \begin{pmatrix} 0.14 & 0 & 0 \\ 0 & -0.07 & 0 \\ 0 & 0 & -0.07 \end{pmatrix}$. The principal components of this tensor were estimated from the experimental data reported by Liu et al.,[10] who measured the swelling strains developed in cubic samples of the present coal matrix material during adsorption of water vapour in the range of 0.1%–95% relative humidity (RH) at 40 °C. Since we assume that the stress state for the pre-compacted powdered samples was hydrostatic, and since that the axial swelling strain measured in our swelling experiments yields the volumetric swelling strain, the term $\exp(\frac{-\sigma'_{ij} A_{ij} V_0}{3RT})$ appearing in Eqs. (1)–(3) and in the function $E(\sigma_{ij}, P_0)$ simplify to unity for the powdered samples.

To estimate the parameter V_0 for water molecules adsorbed in our coal samples, we used the swelling strain measured for P_disc_5 at a low applied axial stress (i.e. at 27.4 MPa where stress driven creep effects are likely to be small) using the expression $V_0 = (\frac{e_v^{eq}}{C\rho})_\sigma$. Here, e_v^{eq} for P_disc_5 at 27.4 MPa applied stress was estimated based on the axial swelling strain e_z^{eq} measured for P_disc_5 at 27.4 MPa, using Eq. (1a), yielding 1.498%, which is similar to the values of 1.37%–1.43% obtained for cubic sample of the same coal matrix material at 95% relative humidity under unconfined conditions.[10] The corresponding adsorbed amount of water (C) at a stress state of 27.4 MPa was estimated as 2.27 mol/kg_{coal} based on the mass difference measured for the sample before and immediately after the experiment. Using the density of our sample P_disc_5 of 1267.2 kg/m³, we obtain $V_0 = 5.21 \times 10^{-6}$ m³/mol for P_disc_5, which is reasonably in line with the average value of 4.3×10^{-6} m³/mol in literature for coals of bituminous rank.[6] We assume this value also holds for the pre-compacted powdered samples.

We now focus on constraining the equilibrium constants for the three models. Since the equilibrium constants K^0, K_1 and K_2, for water adsorption by coal, depend only on temperature and coal rank (in other words, since they are independent of water activity), they can be obtained from best fits of the three models to the experimental data on e_v^{eq} vs. RH, and hence vs. a_g, reported for solid cubic samples by Liu et al.[10] Those data were for the same coal material under unstressed conditions at the same temperature. Fitting the HS model (Model 1) to those data gave $K^0 = 0.161$, whereas the Dent-based swelling model (Model 2) gave $K_1 = 2.236$ and $K_2 = 0.480$, and the DW-based swelling model (Model 3) gave $K_1 = 1.11$ and $K_2 = 0.65$. We assume that these equilibrium constant values for the three models apply for P_disc_5 and for our pre-compacted powdered samples.

Finally, we consider the parameter C_s for the three models. Values of C_s were calculated by fitting equations (1b), (2b) and (3b)

Table 2
Parameter values obtained for the three models used in this study.

Model	C_s (mol/kg$_{coal}$)	K^0	C_{s1} (mol/kg$_{coal}$)	C_{s2} (mol/kg$_{coal}$)	K_1	K_2	V_0 (m³/mol)
P_disc_5 assuming a uniaxial stress state							
1	16.661	0.161					5.21×10^{-6}
2	1.48				2.346	0.480	5.21×10^{-6}
3			1.646	0.326	1.110	0.650	5.21×10^{-6}
P_disc_5 assuming a hydrostatic stress state							
1	17.159	0.161					5.21×10^{-6}
2	1.542				2.346	0.480	5.21×10^{-6}
3			2.737	0.542	1.110	0.650	5.21×10^{-6}
Powdered samples assuming hydrostatic stress states							
1	26.392	0.161					5.21×10^{-6}
2	2.37				2.346	0.480	5.21×10^{-6}
3			4.27	0.833	1.110	0.650	5.21×10^{-6}

to the swelling data obtained at a specific axial reference stress of σ_{ref}, forcing the requirement that $(\varepsilon_{11}^{eq})_{\sigma_{ref}} = (\varepsilon_{11}^{measured})_{\sigma_{ref}}$, where $(\varepsilon_{11}^{eq})_{\sigma_{ref}}$ is the axial swelling strain predicted by the three models at stress σ_{ref}, and where $(\varepsilon_{11}^{measured})_{\sigma_{ref}}$ is the (average) axial swelling strain measured upon introduction of water into our samples at stress σ_{ref}. Here $\sigma_{ref} = 27.4$ MPa for P_disc_5 and 25.9 MPa for pre-compacted powdered sample Powder_1, in line with the choice of the applied stress state for estimation of V_0. The full set of parameter values obtained for the three models for P_disc_5 and the pre-compacted powered samples are summarized in Table 2.

Using the parameters obtained as above, and setting the water activity $a_g = 1$, we applied our three models (Eqs. (1)–(3)) to predict the swelling strains expected for P_disc_5 and the pre-compacted powdered samples versus applied stress states (see Fig. 7). Of course, all three models predict trends that pass through the (average) swelling strains measured experimentally at the reference stresses of 27.4 MPa (sample P_disc_5) and 25.9 MPa (powdered samples), as the models were fitted to these measured data points. It is clear from Fig. 7, that the swelling strains predicted by the three models decrease near-linearly with increasing applied stress, with each model yielding a similar sensitivity of swelling strain to applied stress. The largest reduction in swelling with increasing stress, caused by the thermodynamic stress–strain–sorption effect, is predicted by Model 3 (DW-based swelling model), assuming that the stress state of our samples was hydrostatic. This model predicts (a) that swelling strain decreases from 0.569% to 0.481% for P_disc_5 when the applied stress increases from 27.4 to 100.6 MPa, and (b) that swelling strain decreases from 1.826% to 1.571% for pre-compacted powdered samples when the applied stress increases from 25.9 to 77.8 MPa. However, even using Model 3, the predicted swelling strains are much higher than the measured swelling strains at the same stress. Indeed, Model 3 predicts that the largest sensitivity of swelling strain to hydrostatic stress is -1.2×10^{-3}% strain per MPa for P_disc_5 and -4.9×10^{-3}% strain per MPa for pre-compacted powdered samples. However, the average sensitivity of measured swelling strain to applied stress is around -4.8×10^{-3} to -5.5×10^{-3}% strain per MPa, for P_disc_5, and around -21.1×10^{-3} to 23.2×10^{-3}% strain per MPa for pre-compacted powdered samples (Fig. 7). Taking into account the permanent time-dependent compressive creep strain (i) of ∼0.14% observed for P_disc_5 when the applied stress decreased from 100.6 to 9.2 MPa (Fig. 2(e)), and (ii) of ∼0.84% observed for Powder_1 when the applied stress decreased from 95 to 25.9 MPa (Fig. 3(e)), observed in the stress-stepping compression experiments, the sensitivity of swelling strain to applied stress caused by permanent creep is estimated to be ∼-1.6×10^{-3}% strain per MPa for P_dis_5 and ∼-12×10^{-3}% strain per MPa for the pre-compacted powdered samples. This means that the stress-driven reduction in swelling observed for our samples in the swelling experiments, even after accounting for the permanent

time-dependent deformation (creep) component from our data, is not only due to the thermodynamic effect of stress on water adsorption capacity, but also due to other mechanisms. Specifically, for P_disc_5, around half the reduction in measured swelling can be accounted for by approximately equal contributions from the thermodynamic stress–strain–sorption effect (Models 1–3) plus the permanent strain effect and the other half by a third mechanism. However, for the pre-compacted powdered samples, around $1/2$ the reduction in measured swelling is caused by permanent compaction creep strain effect, while $1/4$ of the reduction can be accounted for by the stress–strain–sorption effect embodied in Models 1–3, meaning that yet another $1/4$ of the reduction is due to a third effect.

Aside from the above, our models can also predict the response expected in the stepwise compression experiments, performed on samples P_disc_5 and Powder_1, due to the thermodynamic effect of stress on water adsorption capacity. These predictions can then be compared with the cumulative time-dependent compression data shown in Figs. 2(e) and 3(e). Such a comparison is shown in Fig. 8, taking the swelling strains predicted by the three models at the lowest applied stress (27.4 MPa for P_disc_5 and 25.9 MPa for pre-compacted powdered samples) employed in the swelling experiments as reference data points, which the models are constrained to pass through, and taking compression as positive. The predicted deformation caused by the thermodynamic stress–strain–sorption effect embodied in Models 1–3 increases near-linearly with increasing applied stress, with the sensitivity to applied stress obtained for P_disc_5 being around 0.3×10^{-3} to 1.1×10^{-3}% strain per MPa, and for Powder_1 being around 2.9×10^{-3} to 3.8×10^{-3}% strain per MPa. The average sensitivity of reversible cumulative time-dependent (compressive) strains versus applied stress measured for P_disc_5 was around 2×10^{-3}% strain per MPa (see unloading data in Fig. 2(e)) and for Powder_1 around 3.1×10^{-3}% strain per MPa (see unloading data in Fig. 3(e)). Therefore, in the compression tests, around $1/2$ of the reversible time-dependent deformation observed for P_disc_5 can be accounted for thermodynamic stress–strain–sorption effect (Models 1–3), and the other half for a third mechanism. For Powder_1, the reversible time-dependent deformation can be fully accounted for thermodynamic stress–strain–sorption effect (Models 1–3)

The above analyses confirm that, in general, the time-dependent deformation exhibited by our samples during exposure to water cannot be explained purely by the thermodynamic stress–strain-sorption effect plus permanent creep, but must also have involved at least one other mechanism. Time-dependent poroelastic effects caused by pore-pressure diffusion process during compaction process may play a role,[39] but would be negligible in this paper, because (a) the pore water pressure used in our experiments is 0.1 MPa only, which corresponds to a total change
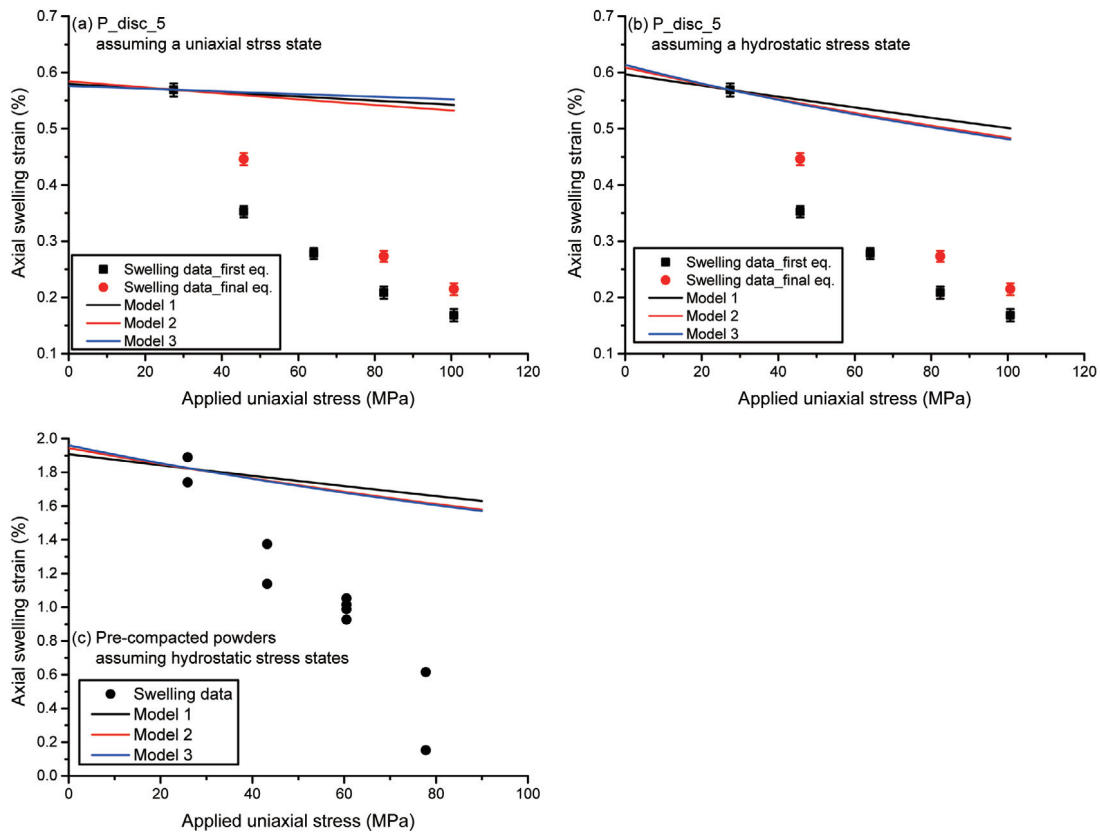
Fig. 7. Comparison of axial swelling strains (%) obtained for our samples versus applied stress, with the predictions of Models 1, 2 and 3 applied for (a) P_disc_5 assuming a uniaxial stress state, (b) P_disc_5 assuming a hydrostatic stress state, and (c) the pre-compacted powdered samples assuming hydrostatic stress states. The dots represent the experimental data shown in Figs. 4 and 5, while the solid lines represent predictions made by the three models as indicated.

in elastic strain of the samples in the order of 0.005%, and therefore the time-dependent poroelastic effects caused by the pore pressure change should be much smaller than the time-dependent strains (in the order of 0.1%) observed in the compaction tests; (b) we calculated the time-dependent compressive strain attained at apparent equilibrium for the wet samples, at stress level i, by subtracting the rapid deformation that occurred within the first 10–20 min at the ith stress state, which may point to that the strains caused by reduction of porosity upon the increase in stress state have been subtracted.

5.1.2. Stress-driven closure of transport paths

Another possible mechanism contributing to the observed stress-driven reduction in swelling of our samples is the stress-driven closure of transport paths in the samples. Closure of the transport paths can potentially occur via the compaction of the coal disc matrix or the matrix within individual grains driven by the applied stress. Closure of the transport paths would reduce access of water into the coal matrix, and hence reduce the swelling measured upon adsorption of water due to equilibrium being established only in accessed portions of the coal matrix. This interpretation is supported by the following evidence.

1. Swelling strains measured for the powered samples were larger than the disc sample. The estimated volumetric swelling of P_disc_5 at the stress state of 27.4 MPa using Eqs. (4a) was 1.5% (see Section 5.1.1), which is less than the measured volumetric swelling strain of ~1.8% for pre-compacted powdered samples at similar stress states (see Fig. 5(b)). This is consistent with our model fits, which show that the calculated values of adsorption site density C_s for P_disc_5 were less than those for pre-compacted powdered samples (see Table 2). The difference in calculated adsorption site density C_s is in turn consistent with the water accessibility to

powdered samples being higher than to the disc sample, as a result of the porosity of powdered samples (~25%) being higher than the disc sample (~4%).

2. The observed swelling kinetics were influenced by the applied stress states. The swelling kinetics data shown in Fig. 6 indicate that swelling rates for pre-compacted powdered samples decreased when the applied stress increased from 25.9 to 43.2 MPa. This is consistent with stress-driven closure of transport paths in individual grains in the pre-compacted powdered samples. On the other hand, the effect was not observed for P_disc_5. This argues against an effect of stress on transport but could also mean that the axial stress acting on sample P_disc_5 mainly closed transport paths in the bedding plane of P_disc_5, thus influencing radial diffusion along the bedding with diameter of 11.8 mm, but with the swelling kinetics being mainly determined by diffusion perpendicular to bedding, as the thickness of P_disc_5 is only 1 mm.

3. Stress-driven reduction of swelling strains measured in our swelling experiments (see Figs. 4(b) and 5(b)) was larger than the cumulative, time-dependent compressive strains measured for wet samples in our compression tests (Figs. 2(e) and 3(e)). In our compression experiments, distilled water was injected into the sample at the lowest applied stress (9.15 MPa for P_disc_5 and 25.93 MPa for Powder_1), while in the swelling experiments it was injected at higher stresses (~25 to ~100 MPa). If applied stress can close transport paths in the coal matrix, and hence reduce water accessibility, then the reduction in swelling strain caused by this mechanism in the swelling experiments should indeed be larger than the cumulative time-dependent deformation, driven by the same mechanism, measured in the compression tests. At the same time, the reduction in swelling strain occurring in swelling tests, caused by the thermodynamic effect of stress and/or permanent creep effect,
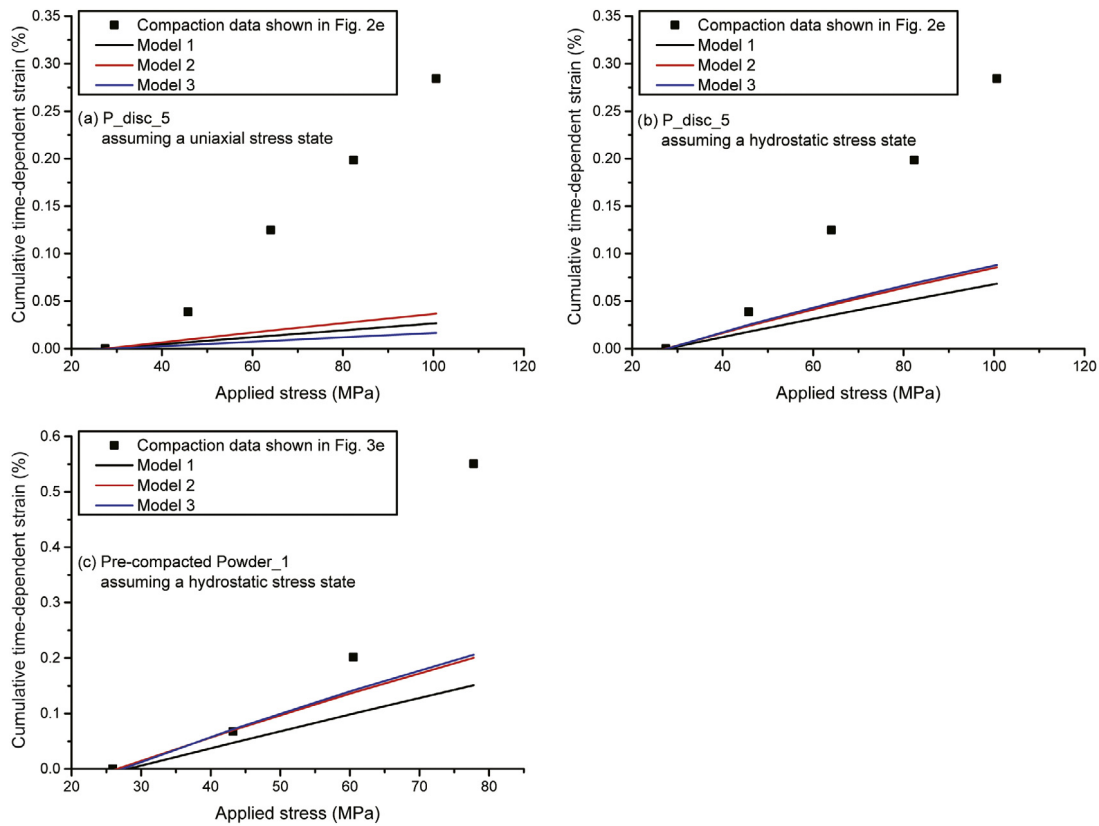
Fig. 8. Comparison of the time-dependent compressive strain (%) versus applied stress data, obtained in our stepwise compression tests, with the predictions of Models 1, 2 and 3 applied for (a) P_disc_5 assuming a uniaxial stress state, (b) P_disc_5 assuming a hydrostatic stress state, and (c) pre-compacted powdered sample Powder_1 assuming a hydrostatic stress state. The dots represent the experimental data shown in Figs. 2(e) and 3(e), while solid lines represent the predictions made by the three models.

should be similar to the cumulative time-dependent compressive strain caused by the same mechanisms occurring for similar stress differences in the compression tests. In Fig. 9, we plot a comparison of the total, stress-driven reduction in swelling strains (Δe_S), obtained in the swelling tests versus the cumulative time-dependent strain data, Δe_D, obtained for water-exposed samples in the compression tests. In the swelling tests, Δe_S is the reduction of swelling strains at a given stress, compared to the reference stress (27.4 MPa for P_disc_5, and 25.9 MPa for the powdered samples). In the compression, Δe_D is the change in cumulative, time-dependent strains at a given stress, compared to the same reference stress. It is clear that $\Delta e_S > \Delta e_D$. Fig. 9 therefore supports the hypothesis that the stress-driven closure of transport paths is one of the mechanisms responsible for stress-driven reduction in swelling in (all) our experiments. Additionally, this also supports that time-dependent poroelastic effects would play little role in controlling mechanisms.

In addition to the above arguments, stress-driven closure of transport paths has also been reported in the literature. Pone et al.[15] measured the CH_4 sorption capacity of bituminous coal (a cylinder of 25 mm in diameter) under both stressed (confined) and unstressed (unconfined) conditions using volumetric methods. They present evidence that confining stresses of 6.9 and 13.8 MPa caused a reduction in CH_4 sorption capacity of 85 and 91% respectively, at a CH_4 pressure of 3.8 MPa at room temperature. Liu et al.[13] showed that this large reduction reported by Pone et al. was due to both (a) a direct effect of stress on equilibrium sorption capacity, and (b) a reduction in the volume of coal sample that was accessible to CH_4 as sample permeability decreased with increasing confining stress.
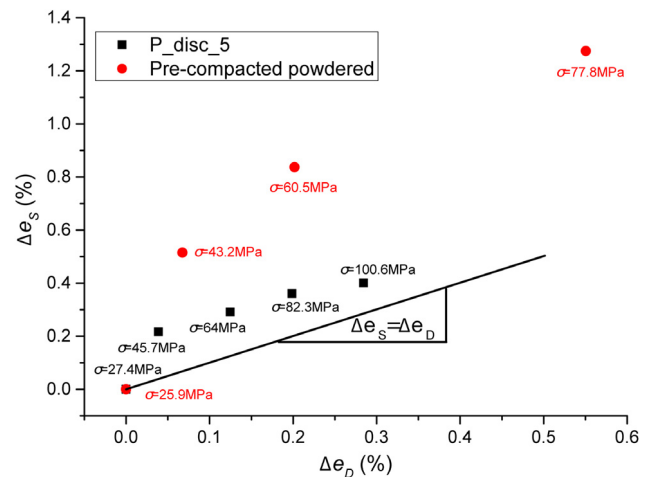

Fig. 9. A comparison of the total, stress-driven reduction in swelling strains (Δe_S), obtained in the swelling tests versus the cumulative time-dependent strain data, Δe_D, obtained for water-exposed samples in the compression tests.

To sum up, the analysis in Sections 5.1.1 and 5.1.2 suggest that the mechanisms responsible for stress-driven reduction in swelling caused by water adsorption are the combined effects of (a) permanent time-dependent deformation (creep), (b) the thermodynamic influence of stress on water adsorption capacity, and c) stress-driven closure of transport paths within the coal matrix material. For the disc sample, mechanism (c) contributed mostly

(see Section 5.1.1), while for powdered samples, mechanism (a) contributed mostly (see Section 5.1.1).

5.2. Comparison of the samples used in the present study: disc versus powders

We have performed experiments on disc sample P_disc_5 and pre-compacted powdered samples. The experimental results consistently showed that applied stress reduces swelling response. However, the results also showed that the disc sample behaved differently in terms of mechanical response under both evacuated and wet conditions, and in terms of swelling behaviour upon introduction of water at constant applied stress, compared with the powdered samples. These differences are compared and analysed as follows.

1. In the evacuated state, Sample P_disc_5 yielded non-linear recoverable/elastic behaviour (see Fig. 2(b)), while the pre-compacted powdered sample Powder_1 yielded near-linear recoverable/elastic behaviour (see Fig. 3(b)). This difference can potentially be explained by the different stress states supported by the disc versus powdered samples under the same or similar uniaxial stress. In the experiments, the true stress state supported by P_disc_5 was likely uniaxial, due to the loose fit in the titanium sample vessel, or perhaps approaching hydrostatic, due to friction generated when the sample deforms laterally against the porous plate. The changes in stress applied to P_disc_5 during loading may well have influenced the uniaxial versus hydrostatic nature of the stress state within the sample, causing the non-linear behaviour observed in the experiments. By contrast, the pre-compacted powdered sample Powder_1 was laterally constrained, so that changes in internal sample stress state during the experiments are likely to have been less marked. In addition to the above, the presence of micro-fractures in Sample P_disc_5 (11.8×1 mm^2) might also lead to the non-linear elastic behaviour observed in our compression experiments, with the apparent stiffness of the sample increasing with increasing applied stress. Compared to P_disc_5 (11.8×1 mm^2), the pre-compacted grains ($180–212$ μm) likely contained fewer or no micro-fractures because the grain size is small.

2. In the water-exposed state, more permanent creep was attained in the pre-compacted powdered sample Powder_1 than in the experiment on P_disc_5 (see Figs. 2(e) and 3(e)). This might be due to (a) the presence of water reducing friction between the grains in the powder sample, promoting rearrangement of the grains, and/or (b) the thus reduced intergranular friction increasing the stresses supported by the grains, hence increasing compaction of the granular samples. These effects might also explain the late stage, time-dependent compaction that occurred in the powdered samples at high stresses in the swelling tests (Fig. 5(a)). They would not be expected to occur in solid sample P_disc_5. This is consistent with the fact that the time-dependent compression was not observed in the swelling experiment on P_disc_5. In addition, the difference observed in permanent compaction between wet P_disc_5 and wet Powder_1 may have been influenced by the stress state in the samples due to the difference in lateral confinement, as postulated for explaining the non-linearity in recoverable/elastic behaviour of P_disc_5 versus Powder_1 under Point 1.

3. Our swelling experiments (Figs. 4 and 5) showed that the volumetric swelling strains measured for the pre-compacted powdered samples were larger than estimated for P_disc_5 at similar applied stresses. This can be explained by (a) greater water accessibility to the coal matrix in the powdered samples than in P_disc_5 (also see 5.1.2 point 1), or (b) faster equilibration or a higher level of equilibration in the powdered samples than in P_disc_5.

Based on the above analysis, it is inferred that the differences in mechanical response between the disc and powdered samples are mainly caused by differences in pore structure, for example the presence of microfractures in P_disc_5 versus the large intergranular porosity of the powdered samples with an absence of microfractures within the grains. In other words, the pore structure of the samples played an important role in controlling their response to loading and presence of water.

5.3. Effect of water on mechanical response of the samples

Our stepwise compression test data visible in Figs. 2 and 3 show that the presence of water changed the mechanical response of both the disc and powdered samples to loading. Compared to the samples loaded in the evacuated state, incremental loading of the wet samples involved a reversible component of time-dependent deformation plus permanent creep. These effects influenced the apparent elastic modulus of the samples in the presence of water, as seen from a comparison of the strain–stress curves shown in Fig. 2(b) and (d), for P_disc_5, and in Fig. 3(b) and (d), for Powder_1. These figures show there was a minor influence of water on the apparent modulus in the case of P_disc_5, but a large influence in the case of Powder_1.

Focusing now on the reversible component of time-dependent compaction, we have already inferred in Section 5.1. that this reversible component of deformation during stepwise loading is controlled by the thermodynamic stress–strain–sorption effect plus the closure of transport paths driven by elastic deformation. The permanent creep component observed in the present experiments might also be related to the presence of water, again as already discussed. For example, in the powdered samples, the presence of water might reduce friction between the grains, thus resulting in the permanent compaction creep due to either rearrangement of grains or an increase in stress supported by the grains (see also Section 5.2). On the other hand, in sample P_disc_5, microfractures could be generated due to sorption and swelling,[43] and thus cumulative microcracking could potentially cause or promote permanent compaction creep.

5.4. Likely implications for (E)CBM

Our findings have a number of implications for (E)CBM production. These can be summarized as follows.

First, our models predict that applied stress reduces water sorption capacity and associated swelling, and this effect depends on the magnitude of partial volume of adsorbed molecules (V_0). In the case of the Brzeszcze high volatile bituminous coal samples used in the present study, the estimated V_0 is small (5.21×10^{-6} m^3/mol), and the thermodynamic effect of stress on water adsorption capacity, and the resulting reduction in swelling (see Fig. 7), are small and can be neglected at in-situ, lithostatic stress states (which typically lie in the range 10–30 MPa). However, as V_0 for adsorbed water molecules in principle depends on coal rank, for lower rank coal with a generally higher value of V_0 (e.g. $V_0 = 13 \times 10^{-6}$ m^3/mol for lignite[7]), the thermodynamic effect of in-situ stress on water adsorption capacity and on the associated swelling might have to be considered when designing and optimizing enhanced (E)CBM production strategies.

Second, in the case of Brzeszcze high volatile bituminous coal, our experiments show volumetric swelling strains caused by water adsorption (at 100% relative humidity) of ~1.5 to ~1.8% at applied axial stresses of ~25 MPa (equivalent to an in-situ burial depth of ~1000 m). These swelling strains are similar to the volumetric swelling strains (1.37%–1.43%) measured for similar Brzeszcze coal matrix samples at 95% relative humidity under unconfined conditions.[10] This suggests that effects of permanent creep and closure of intra-matrix transport paths, driven by in-situ stress, on the swelling behaviour of coals like the Brzeszcze coal are also small enough to be negligible in practice. This is further supported

by the fact that our experiments on the disc sample was not fully confined laterally and the powdered samples had high intergranular porosity, so that larger creep strains were likely possible than would occur in dense coal under in-situ conditions.

Finally, the present results have shown that the effect of lithostatic stress on the swelling/shrinkage response of coal to water is minor and for practical purposes negligible for Brzeszcze high volatile bituminous coal. This means that the large shrinkage effects due to drying seen in the unconfined experiments[10] are not changed by in-situ stresses. The implication is that the (E)CBM strategy, proposed by Liu et al.[10] (i.e. of removing water from coal seams by nitrogen flushing thus initiating self-enhancing shrinkage and (micro)cracking of the coal and enhanced methane production) is not significantly influenced by effects of in-situ stress on swelling/sorption.

6. Conclusions

In an attempt to understand the effect of applied stress on water adsorption by coal and on the associated swelling, thermodynamic models for swelling of coal matrix material due to water adsorption under stressed conditions were developed, assuming three adsorption mechanisms (i.e. mono-layer adsorption, multiple-layer adsorption, and the combined mono- plus multiple-layer adsorption). Our models predict that applied stresses reduce water sorption capacity and the associated swelling. In addition, experiments were performed on both a solid disc and on pre-compacted powders of Brzeszcze high volatile bituminous coal at a constant temperature of 40 °C, using a uniaxial compaction apparatus. The mechanical response of the samples to stepwise axial loading was determined under both evacuated (i.e. 0% relative humidity) and water-exposed (i.e. 100% relative humidity) conditions. The evacuated samples showed reversible, elastic behaviour. Water-exposed samples exhibited elastic deformation, time-dependent reversible deformation, plus permanent compaction creep. Axial swelling strains due to introduction of distilled water (i.e. 100% relative humidity) at a constant fluid pressure of 0.1 MPa were also measured for samples subjected to fixed axial stress states applied in the range of 25–100 MPa. The experimental results demonstrate that swelling due to water adsorption is reduced by increasing applied stress. Comparison with predictions made using the three models investigated suggests that stress-driven reduction in sorption-induced swelling is not caused solely by the thermodynamic effect of a stress-driven reduction in water adsorption capacity. Permanent creep also occurred. Another likely mechanism contributing to the stress-driven reduction in swelling is the stress-driven closure of the transport paths. In summary, this means that the stress-driven reduction in swelling upon adsorption of water is caused by the combined effects of (a) permanent compaction creep, (b) the thermodynamic effect of a stress-driven reduction in water sorption capacity and (c) stress-driven closure of the transport paths. For the disc sample, mechanism (c) led to around half the reduction of swelling, while the other mechanisms contributed equally to the remaining reduction. For powdered samples, mechanism (a) led to about half the reduction of swelling, while mechanisms (a) and (b) contributed roughly equally to the remainder. Nonetheless, our results have shown only minor effects of stress on the swelling response of (Brzeszcze) high volatile bituminous coal to water at typical in-situ stresses of 10–30 MPa. This means that large shrinkage effects due to drying seen in unconfined experiments is not changed by in-situ stresses. The implication is that under in-situ (E)CBM conditions, removing water from coal seams, for example by flushing with dry N_2, can potentially initiate self-enhancing shrinkage and (micro)cracking of the coal, thus enhancing methane production.

Appendix A. Model development

The effects of stress on adsorption by Mechanism I has already been explored by Hol et al.,[3] and by Liu et al.,[13] assuming that general states of stress are supported by the coal matrix material. These authors arrived at general stress–strain–sorption relations for monolayer adsorption of any sorbate species. To date, however, the Dent and the DW models have only been developed and applied for describing water adsorption by unstressed coal, i.e. for describing sorbed water concentration versus RH or relative pressure in the case of unstressed coal. Here, we will review the monolayer models derived by Hol, Liu and co-workers, identifying how stress supported by a solid sorbent influences sorption site occupancy in general. We then apply this result to extend the Dent and DW sorption models to obtain stress–strain–sorption relations for the multilayer sorption mechanisms that they represent (Mechanisms 2 and 3, respectively).

A.1. Model 1: Monolayer sorption/swelling model (modified Hol and Spiers model)

For monolayer sorption of a pure sorbate species such as CH_4, CO_2, N_2 or H_2O, Liu et al.[13] gave the potential of the adsorbed molecules in stressed sorbent (coal) matrix material, expressed in J/mol, as

$$\mu_s = \mu_s^{P_0} + RT \ln(\frac{\theta}{1-\theta}) + (\overline{\sigma} - P_0 + \frac{1}{3}\sigma'_{ij}A_{ij})V_0. \qquad (A.1)$$

Here, the quantity $\mu_s^{P_0}$ (J/mol) represents the potential of the adsorbed molecules at a reference pressure $P_0 = 0.1$ MPa. This depends solely on temperature for a given sorption reaction. The quantity θ represents the concentration of adsorbed gas measured in terms of primary/monolayer adsorption site occupancy, T (K) is the thermodynamic (absolute) temperature, R ($J \cdot K^{-1} \cdot mol^{-1}$) is the gas constant, and the term $R \ln(\frac{\theta}{1-\theta})$ is the molar configurational entropy of the adsorbed molecules. In addition, V_0 (m^3/mol) represents the partial molar volume of the adsorbed gas molecules, A_{ij} is a second rank tensor representing the swelling strain anisotropy (see details in Liu et al.[13]), and the term $(\overline{\sigma} + \frac{1}{3}\sigma'_{ij}A_{ij} - P_0) V_0$ represents the stress–strain work done on the surroundings as coal swells against the stress σ_{ij} in excess of the reference pressure of P_0, i.e. $(\sigma_{ij} - P_0\delta_{ij})$, when one mole of sorbate molecules are adsorbed. It is clearly seen from Eq. (A.1) that the chemical potential depends not only on the adsorbed occupancy, but also on the stress–strain work done. It is also clear that the magnitude of the stress effect on the chemical potential depends on the partial molar volume of the adsorbed molecules V_0.

At equilibrium, the chemical potential of the adsorbed molecules (μ_s) must be equal to that of the gas molecules ($\mu_g = \mu_{g0} + RT \ln a_g$). Setting Eq. (A.1) equal to μ_g then yields the following relationship for the sorption capacity C (mol/kg$_{coal}$) of the stressed coal matrix[13]:

$$C = C_s\theta$$

$$= \frac{C_s a_g \exp(\frac{\mu_{g0}-\mu_s^{P_0}}{RT}) \exp(\frac{-(\overline{\sigma}-P_0)V_0}{RT}) \exp(\frac{-\sigma'_{ij}A_{ij}V_0}{3RT})}{1 + a_g \exp(\frac{\mu_{g0}-\mu_s^{P_0}}{RT}) \exp(\frac{-(\overline{\sigma}-P_0)V_0}{RT}) \exp(\frac{-\sigma'_{ij}A_{ij}V_0}{3RT})}. \qquad (A.2a)$$

Here C_s (mol/kg$_{coal}$) represents the total number of localized adsorption sites (in mol) present in one kilogramme of coal matrix, a_g

represents the activity of gas at given PT conditions, μ_{g0} represents the chemical potential of gas molecules at a reference pressure $P_0 = 0.1$ MPa, and the term $\exp(\frac{\mu_{g0}-\mu_s^{P_0}}{RT})$ is the equilibrium constant K^0 for the sorption reaction, which depends solely on temperature. From Eqs. (A.1) and (A.2), it is clear, while that the term $(\overline{\sigma} - P_0 + \frac{1}{3}\sigma'_{ij}A_{ij})V_0$ expresses the stress–strain work done on the surroundings as coal swells against the stress $(\sigma_{ij} - P_0\delta_{ij})$, the term $E(\sigma_{ij}, P_0) = \exp(\frac{-(\overline{\sigma}-P_0)V_0}{RT})\exp(\frac{-\sigma'_{ij}A_{ij}V_0}{3RT})$ expresses the reduction in adsorption site occupancy caused by the applied stress in excess of the reference pressure P_0.

Note that when sorption-induced swelling is negligible (i.e. $V_0 \to 0$) or when no stress is applied to the solid framework in excess of P_0, Eq. (A.2a) reduces to

$$C = \frac{C_s a_g K^0}{1 + a_g K^0}. \tag{A.2b}$$

This is the well-known Langmuir equation,[44] which is classically derived assuming that there is no sorption-induced swelling ($V_0 = 0$), expressed in terms of gas activity. When the coal matrix is subjected to a hydrostatic stress $\sigma(\sigma > P_0)$ or a gas pressure of the same magnitude, Eq. (A.2a) becomes[13]

$$C = C_s\theta = \frac{C_s a_g K^0 \exp(\frac{-(\sigma-P_0)V_0}{RT})}{1 + a_g K^0 \exp(\frac{-(\sigma-P_0)V_0}{RT})}. \tag{A.2c}$$

Assuming now that V_0 is insensitive to both adsorbed concentration and the applied stress states, and that the swelling of coal matrix upon adsorption is caused by V_0, the volumetric swelling strain (e_v^{eq}) of the stressed coal upon adsorption is given from the above as

$$e_v^{eq} = C\rho V_0 \tag{A.3a}$$

$$\text{or} \quad e_v^{eq} = \rho V_0 C_s \frac{a_g K^0 \exp(\frac{-(\overline{\sigma}-P_0)V_0}{RT})\exp(\frac{-\sigma'_{ij}A_{ij}V_0}{3RT})}{1 + a_g K^0 \exp(\frac{-(\overline{\sigma}-P_0)V_0}{RT})\exp(\frac{-\sigma'_{ij}A_{ij}V_0}{3RT})} \tag{A.3b}$$

$$\text{or} \quad e_v^{eq} = \rho V_0 C_s \frac{a_g K^0 E(\sigma_{ij}, P_0)}{1 + a_g K^0 E(\sigma_{ij}, P_0)}. \tag{A.3c}$$

Similarly, the full strain tensor representing the general, anisotropic adsorption–induced, swelling response of coal subjected to a general stress state σ_{ij} is given

$$\varepsilon_{ij}^{eq} = \frac{A_{ij} + \delta_{ij}}{3}e_v^{ads} = \frac{A_{ij} + \delta_{ij}}{3}C\rho V_0 \tag{A.4a}$$

$$\text{or} \quad \varepsilon_{ij}^{eq} = \frac{A_{ij} + \delta_{ij}}{3}\rho V_0 C_s \frac{a_g K^0 E(\sigma_{ij}, P_0)}{1 + a_g K^0 E(\sigma_{ij}, P_0)}. \tag{A.4b}$$

The effect of applied stress on adsorbed concentration and the associated swelling embedded in the occupancy reduction term $E(\sigma_{ij}, P_0) = \exp(\frac{-(\overline{\sigma}-P_0)V_0}{RT})\exp(\frac{-\sigma'_{ij}A_{ij}V_0}{3RT})$ forms the physical basis for the models developed in this paper for swelling of stressed coal matrix material upon adsorption of water.

A.2. Model 2: Dent-based swelling model

Dent[35] assumed that the thermodynamic properties of water molecules adsorbed primarily by coal are different to those adsorbed secondarily, and applied the well-known the Brunauer–Emmett–Teller (BET) model for multiple layer adsorption[45] to describe the corresponding sorption behaviour. Writing the partial pressure of water in terms of water activity (a_g), the resulting Dent variant of the BET model can be expressed as

$$C = C_1 + C_2$$
$$= \frac{C_s K_1 a_g}{1 - K_2 a_g + K_1 a_g} + \frac{C_s K_1 K_2 a_g^2}{(1 - K_2 a_g)(1 - K_2 a_g + K_1 a_g)} \tag{A.5}$$

where C_1 (mol/kg$_{coal}$) and C_2 (mol/kg$_{coal}$) represent the concentration of water molecules adsorbed in primary and secondary adsorption sites at equilibrium, and where K_1 and K_2 represent the equilibrium constants for primary adsorption and secondary adsorption. If no secondary adsorption occurs, the Dent model reduces to the single layer Langmuir model expressed in terms of gas activity, i.e. Eq. (A.5) reduces to (A.2b).

Applying the analysis above for the effect of stress on site occupancy for single layer sorption, and extending this to the thermodynamically analogous case of secondary adsorption, the Dent model for water adsorption by stressed coal matrix material becomes

$$C = C_1 + C_2$$
$$= \frac{C_s K_1 E(\sigma_{ij}, P_0)a_g}{1 - K_2 E(\sigma_{ij}, P_0)a_g + K_1 E(\sigma_{ij}, P_0)a_g} \tag{A.6}$$
$$+ \frac{C_s K_1 K_2 E^2(\sigma_{ij}, P_0)a_g^2}{(1 - K_2 E(\sigma_{ij}, P_0)a_g)(1 - K_2 E(\sigma_{ij}, P_0)a_g + K_1 E(\sigma_{ij}, P_0)a_g)}.$$

Inserting Eq. (6) into (3a) and (4a), the following results are hence obtained for the swelling of coal matrix material due to multiple layer adsorption of water under stressed conditions:

$$e_v^{eq} = \rho V_0 C_s$$
$$\times \left\{ \begin{array}{c} \dfrac{K_1 E(\sigma_{ij}, P_0)a_g}{1 - K_2 E(\sigma_{ij}, P_0)a_g + K_1 E(\sigma_{ij}, P_0)a_g} \\ + \dfrac{K_1 K_2 E^2(\sigma_{ij}, P_0)a_g^2}{[1 - K_2 E(\sigma_{ij}, P_0)a_g][1 - K_2 E(\sigma_{ij}, P_0)a_g + K_1 E(\sigma_{ij}, P_0)a_g]} \end{array} \right\} \tag{A.7a}$$

$$\varepsilon_{ij}^{eq} = \frac{A_{ij} + \delta_{ij}}{3}\rho V_0 C_s$$
$$\times \left\{ \begin{array}{c} \dfrac{K_1 E(\sigma_{ij}, P_0)a_g}{1 - K_2 E(\sigma_{ij}, P_0)a_g + K_1 E(\sigma_{ij}, P_0)a_g} \\ + \dfrac{K_1 K_2 E^2(\sigma_{ij}, P_0)a_g^2}{[1 - K_2 E(\sigma_{ij}, P_0)a_g][1 - K_2 E(\sigma_{ij}, P_0)a_g + K_1 E(\sigma_{ij}, P_0)a_g]} \end{array} \right\}. \tag{A.7b}$$

A.3. Model 3: DW-based swelling model

The D'Arcy and Watt (DW) model[20,21,37,46] was formulated as a combination of the Langmuir isotherm for monolayer adsorption with strong binding energy,[44] and the Dubinin and Serpinsky (DS1) isotherm for multiple-layer adsorption.[32] Upon replacing the partial pressure of water vapour by the activity of water vapour, the result obtained by D'Arcy and Watt can be expressed as

$$C = \frac{C_{s1} K_1 a_g}{1 + K_1 a_g} + \frac{C_{s2} K_2 a_g}{1 - K_2 a_g}. \tag{A.8}$$

Here C_{s1} and C_{s2} (mol/kg$_{coal}$) represent the number of localized adsorption sites (in mol) present in one kilogramme of coal matrix for monolayer adsorption and for multiple-layer adsorption, respectively, while the quantities K_1 and K_2 represent the corresponding equilibrium constants. If only single layer adsorption occurs, the model reduces to the Langmuir type equation, of course (c.f. Eq. (A.2b)).

Again applying the term $E(\sigma_{ij}, P_0)$ to account for the effects of stress on both primary and secondary site occupancy, we modified the DW model for water adsorption by the stressed coal to obtain

$$C = \frac{C_{s1} K_1 E(\sigma_{ij}, P_0)a_g}{1 + K_1 E(\sigma_{ij}, P_0)a_g} + \frac{C_{s2} K_2 E(\sigma_{ij}, P_0)a_g}{1 - K_2 E(\sigma_{ij}, P_0)a_g}. \tag{A.9}$$

Inserting Eq. (A.9) into (A.3a) and (A.4a), we obtain our Model 3 for swelling of coal matrix material due to adsorption of water, i.e.

$$e_v^{eq} = \rho V_0 \left\{ \frac{C_{s1} K_1 E(\sigma_{ij}, P_0)a_g}{1 + K_1 E(\sigma_{ij}, P_0)a_g} + \frac{C_{s2} K_2 E(\sigma_{ij}, P_0)a_g}{1 - K_2 E(\sigma_{ij}, P_0)a_g} \right\} \tag{A.10a}$$

and $\quad \varepsilon_{ij}^{eq} = \dfrac{A_{ij} + \delta_{ij}}{3} \rho V_0$

$$\times \left\{ \frac{C_{s1} K_1 E(\sigma_{ij}, P_0) a_g}{1 + K_1 E(\sigma_{ij}, P_0) a_g} + \frac{C_{s2} K_2 E(\sigma_{ij}, P_0) a_g}{1 - K_2 E(\sigma_{ij}, P_0) a_g} \right\}. \quad \text{(A.10b)}$$

Appendix B

B.1. Compression test calibrations

The loading frame and compaction cell pistons inevitably experience elastic deformation when load is applied to any sample (apparatus compressibility effect). To obtain the true deformation of the sample versus loading stress (in the compression experiments), the displacement measurements obtained from the external LVDT was corrected using apparatus distortion calibrations. Apparatus distortion or compliance was calibrated by cyclic loading under conditions identical to those used in the compression experiments, with no sample being present. Based on a linear fit ($R^2 > 0.99$) to the external LVDT data versus axial load data, apparatus compliance was obtained. We also note that friction between the loading pistons and O-rings was negligible as the O-rings supported a max pressure difference of only 0.1 MPa (1 atm) in the evacuated condition.

B.2. Swelling test calibrations

In our swelling tests at a constant load, the introduction of liquid water into the evacuated sample, at a fluid pressure of 0.1 MPa, causes a change in applied stress states that leads to minor deformation of the apparatus. This deformation was calibrated by measuring the change in external LVDT signal due to introduction of 0.1 MPa liquid water at loading force 1 kN, 3 kN and 5 kN, without sample being present. The results yielded a small, rapid, time-independent deformation, which was insensitive to load. The magnitude corresponded to a swelling displacement of around 0.75 μm, which means a 0.075% (absolute) swelling strain of the 1 mm thick coal disc, and 0.04–0.06% (absolute) strain of the coal powder samples. This was used to correct our experimental data where significant. As in the compression tests, O-ring friction effects were of course negligible in the swelling tests. Friction at the interface between sample and titanium compaction vessel were inferred to be negligible too, as graphite-lubricated test runs yielded the same results as runs without graphite.

References

1. Laubach S, Marrett R, Olson J, Scott A. Characteristics and origins of coal cleat: A review. *Int J Coal Geol.* 1998;35:175–207.
2. Levine JR. Model study of the influence of matrix shrinkage on absolute permeability of coal bed reservoirs. *Geol Soc Lond Spec Publ.* 1996;109:197–212.
3. Hol S, Peach CJ, Spiers CJ. Effect of 3-D stress state on adsorption of CO_2 by coal. *Int J Coal Geol.* 2012;93:1–15. http://dx.doi.org/10.1016/j.coal.2012.01.001.
4. White CM, et al. Sequestration of carbon dioxide in coal with enhanced coalbed methane recovery a review. *Energy Fuels.* 2005;19:659–724.
5. Moore TA. Coalbed methane: A review. *Int J Coal Geol.* 2012;101:36–81.
6. Fry R, Day S, Sakurovs R. Moisture-induced swelling of coal. *Int J Coal Prep Util.* 2009;29:298–316.
7. Suuberg EM, Otake Y, Yun Y, Deevi SC. Role of moisture in coal structure and the effects of drying upon the accessibility of coal structure. *Energy Fuels.* 1993;7:384–392.
8. Pan Z. Modeling of coal swelling induced by water vapor adsorption. *Front Chem Sci Eng.* 2012;6:94–103.
9. Day S, Fry R, Sakurovs R. Swelling of moist coal in carbon dioxide and methane. *Int J Coal Geol.* 2011;86:197–203.
10. Liu J, Peach CJ, Spiers CJ. Anisotropic swelling behaviour of coal matrix cubes exposed to water vapour: Effects of relative humidity and sample size. *Int J Coal Geol.* 2016;167:119–135.
11. Day S, Fry R, Sakurovs R, Weir S. Swelling of coals by supercritical gases and its relationship to sorption. *Energy Fuels.* 2010;24:2777–2783. http://dx.doi.org/10.1021/Ef901588h.
12. Day S, Fry R, Sakurovs R. Swelling of coal in carbon dioxide, methane and their mixtures. *Int J Coal Geol.* 2012;93:40–48. http://dx.doi.org/10.1016/j.coal.2012.01.008.
13. Liu J, Spiers CJ, Peach CJ, Vidal-Gilbert S. Effect of lithostatic stress on methane sorption by coal: Theory vs. experiment and implications for predicting in-situ coalbed methane content. *Int J Coal Geol.* 2016;167:48–64.
14. Liu J, Peach CJ, Zhou H, Spiers CJ. Thermodynamic models for swelling of unconfined coal due to adsorption of mixed gases. *Fuel.* 2015;157:151–161. http://dx.doi.org/10.1016/j.fuel.2015.04.070.
15. Pone JDN, Halleck PM, Mathews JP. Sorption capacity and sorption kinetic measurements of CO_2 and CH_4 in confined and unconfined bituminous coal. *Energy Fuels.* 2009;23:4688–4695. http://dx.doi.org/10.1021/ef9003158.
16. Hol S, Peach CJ, Spiers CJ. Applied stress reduces the CO_2 sorption capacity of coal. *Int J Coal Geol.* 2011;85:128–142. http://dx.doi.org/10.1016/j.coal.2010.10.010.
17. Vandamme M, Brochard L, Lecampion B, Coussy O. Adsorption and strain: the CO_2-induced swelling of coal. *J Mech Phys Solids.* 2010;58:1489–1505.
18. Busch A, Gensterblum Y. CBM and CO_2-ECBM related sorption processes in coal: A review. *Int J Coal Geol.* 2011;87:49–71. http://dx.doi.org/10.1016/j.coal.2011.04.011.
19. Yu J, Tahmasebi A, Han Y, Yin F, Li X. A review on water in low rank coals: the existence, interaction with coal structure and effects on coal utilization. *Fuel Process Technol.* 2013;106:9–20.
20. Švábová M, Weishauptová Z, Přibyl O. Water vapour adsorption on coal. *Fuel.* 2011;90:1892–1899.
21. McCutcheon AL, Barton WA, Wilson MA. Characterization of water adsorbed on bituminous coals. *Energy Fuels.* 2003;17:107–112.
22. Charrière D, Behra P. Water sorption on coals. *J Colloid Interface Sci.* 2010;344:460–467.
23. Cui X, Bustin RM, Dipple G. Selective transport of CO_2, CH_4, and N_2 in coals: insights from modeling of experimental gas adsorption data. *Fuel.* 2004;83:293–303.
24. Day S, Sakurovs R, Weir S. Supercritical gas sorption on moist coals. *Int J Coal Geol.* 2008;74:203–214. http://dx.doi.org/10.1016/j.coal.2008.01.003.
25. Danesh NN, et al. Impact of creep on the evolution of coal permeability and gas drainage performance. *J Nat Gas Sci Eng.* 2016;33:469–482.
26. Liu J, Fokker PA, Spiers CJ. Coupling of swelling, internal stress evolution, and diffusion in coal matrix material during exposure to methane. *J Geophys Res Solid Earth.* 2017;122:844–865.
27. Hol S, Spiers CJ. Competition between adsorption-induced swelling and elastic compression of coal at CO_2 pressures up to 100 MPa. *J Mech Phys Solids.* 2012;60:1862–1882.
28. Mu R, Malhotra V. A new approach to elucidate coal-water interactions by an in situ transmission FT-ir technique. *Fuel.* 1991;70:1233–1235.
29. Kaji R, Muranaka Y, Otsuka K, Hishinuma Y. Water absorption by coals: effects of pore structure and surface oxygen. *Fuel.* 1986;65:288–291.
30. Suárez N, Laredo E, Nava R. Characterization of four hydrophilic sites in bituminous coal by ionic thermal current measurements. *Fuel.* 1993;72:13–18.
31. Dubinin M. Water vapor adsorption and the microporous structures of carbonaceous adsorbents. *Carbon.* 1980;18:355–364.
32. Dubinin M, Serpinsky V. Isotherm equation for water vapor adsorption by microporous carbonaceous adsorbents. *Carbon.* 1981;19:402–403.
33. Nishino J. Adsorption of water vapor and carbon dioxide at carboxylic functional groups on the surface of coal. *Fuel.* 2001;80:757–764.
34. Lynch LJ, Webster DS. Effect of thermal treatment on the interaction of brown coal and water: a nuclear magnetic resonance study. *Fuel.* 1982;61:271–275.
35. Dent R. A multilayer theory for gas sorption part I: sorption of a single gas. *Text Res J.* 1977;47:145–152.
36. D'Arcy R, Watt I. Analysis of sorption isotherms of non-homogeneous sorbents. *Trans Faraday Soc.* 1970;66:1236–1245.
37. Barton S, Evans M, MacDonald J. Adsorption of water vapor on nonporous carbon. *Langmuir.* 1994;10:4250–4252.
38. Liteanu E, Spiers CJ. Influence of pore fluid salt content on compaction creep of calcite aggregates in the presence of supercritical CO_2. *Chem Geol.* 2009;265:134–147.
39. Espinoza D, Vandamme M, Dangla P, Pereira J-M, Vidal-Gilbert S. Adsorptive-mechanical properties of reconstituted granular coal: Experimental characterization and poromechanical modeling. *Int J Coal Geol.* 2016;162:158–168.
40. Li D, et al. High-pressure sorption isotherms and sorption kinetics of CH_4 and CO_2 on coals. *Fuel.* 2010;89:569–580.
41. Staib G, Sakurovs R, Gray EMA. A pressure and concentration dependence of CO_2 diffusion in two Australian bituminous coals. *Int J Coal Geol.* 2013;116:106–116.

42. Staib G, Sakurovs R, Gray EM. Kinetics of coal swelling in gases: Influence of gas pressure, gas type and coal type. *Int J Coal Geol.* 2014;132:117–122.

43. Hol S, Spiers CJ, Peach CJ. Microfracturing of coal due to interaction with CO_2 under unconfined conditions. *Fuel.* 2012;97:569–584.

44. Langmuir I. The adsorption of gases on plane surfaces of glass, mica and platinum. *J Am Chem Soc*. 1918;40:1361–1403.

45. Brunauer S, Emmett PH, Teller E. Adsorption of gases in multimolecular layers. *J Am Chem Soc*. 1938;60:309–319.

46. Furmaniak S, Gauden PA, Terzyk AP, Rychlicki G. Water adsorption on carbons — critical review of the most popular analytical approaches. *Adv Colloid Interface Sci*. 2008;137:82–143.